ELEMENTA
Science of the Anthropocene

Freshwater distributions and water mass structure in the Amundsen Sea Polynya region, Antarctica

E. Randall-Goodwin[1] • M. P. Meredith[2] • A. Jenkins[2] • P. L. Yager[3] • R. M. Sherrell[4,7] • E. P. Abrahamsen[2] • R. Guerrero[5] • X. Yuan[6] • R. A. Mortlock[7] • K. Gavahan[8] • A.-C. Alderkamp[9] • H. Ducklow[6] • R. Robertson[10] • S. E. Stammerjohn[11]*

[1]Scripps Institution of Oceanography, University of California, San Diego, California, United States
[2]British Antarctic Survey, Natural Environment Research Council, Cambridge, United Kingdom
[3]Department of Marine Sciences, University of Georgia, Athens, Georgia, United States
[4]Department of Marine and Coastal Sciences, Rutgers University, New Brunswick, New Jersey, United States
[5]Physical Oceanography Program, Instituto Nacional de Investigacion y Desarrollo Pesquero, Mar del Plata, Argentina
[6]Lamont-Doherty Earth Observatory, Columbia University, New York, New York, United States
[7]Department of Earth and Planetary Sciences, Rutgers University, Piscataway, New Jersey, United States
[8]Antarctic Support Contract, Centennial, Colorado, United States
[9]Department of Environmental Earth System Science, Stanford University, Stanford, California, United States
[10]School of Physical, Environmental, and Mathematical Sciences, University of New South Wales Canberra, the Australian Defence Force Academy, Canberra, ACT, Australia
[11]Institute of Arctic and Alpine Research, University of Colorado, Boulder, Colorado, United States

*sharon.stammerjohn@colorado.edu

Abstract

We present the first densely-sampled hydrographic survey of the Amundsen Sea Polynya (ASP) region, including a detailed characterization of its freshwater distributions. Multiple components contribute to the freshwater budget, including precipitation, sea ice melt, basal ice shelf melt, and iceberg melt, from local and non-local sources. We used stable oxygen isotope ratios in seawater ($\delta^{18}O$) to distinguish quantitatively the contributions from sea ice and meteoric-derived sources. Meteoric fractions were high throughout the winter mixed layer (WML), with maximum values of 2–3% (±0.5%). Because the ASP region is characterized by deep WMLs, column inventories of total meteoric water were also high, ranging from 10–13 m (±2 m) adjacent to the Dotson Ice Shelf (DIS) and in the deep trough to 7–9 m (±2 m) in shallower areas. These inventories are at least twice those reported for continental shelf waters near the western Antarctic Peninsula. Sea ice melt fractions were mostly negative, indicating net (annual) sea ice formation, consistent with this area being an active polynya. Independently determined fractions of subsurface glacial meltwater (as one component of the total meteoric inventory) had maximum values of 1–2% (±0.5%), with highest and shallowest maximum values at the DIS outflow (80–90 m) and in iceberg-stirred waters (150–200 m). In addition to these upwelling sites, contributions of subsurface glacial meltwater could be traced at depth along the ~ 27.6 isopycnal, from which it mixes into the WML through various processes. Our results suggest a quasi-continuous supply of melt-laden iron-enriched seawater to the euphotic zone of the ASP and help to explain why the ASP is Antarctica's most biologically productive polynya per unit area.

Domain Editor-in-Chief
Jody W. Deming, University of Washington

Associate Editor
Edward C. Carmack, Fisheries & Oceans Canada

Knowledge Domain
Ocean Science

Article Type
Research Article

Part of an *Elementa* Special Feature
ASPIRE: The Amundsen Sea Polynya International Research Expedition

Received: November 28, 2014
Accepted: July 8, 2015
Published: August 7, 2015

Introduction

The Amundsen Sea Polynya (ASP; Figure 1) is the most biologically productive polynya (per unit area) in Antarctica (Arrigo and van Dijken, 2003). At the same time, many of the ice shelves of the Amundsen Sea embayment are experiencing basal melt rates that are high enough to drive ice shelf thinning (Paolo et al.,

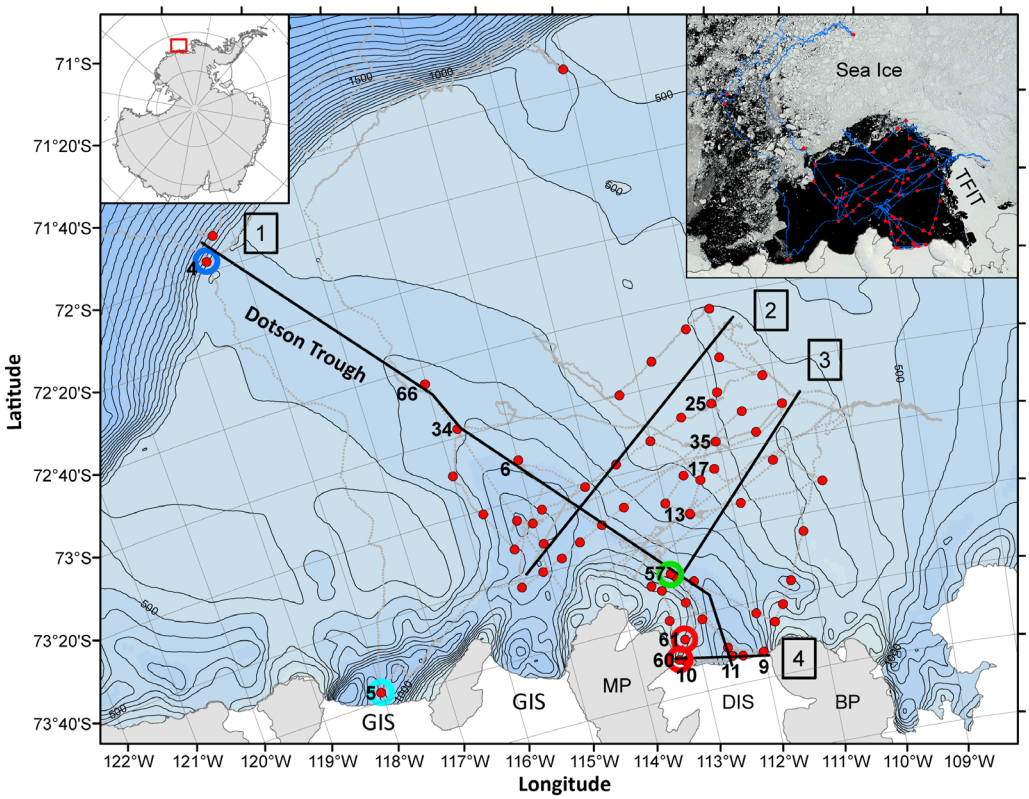

Figure 1

ASPIRE station locations and regional bathymetry.

Locations of CTD observations acquired during ASPIRE (NBP10-05), overlain on regional bathymetry (blue shading and dark gray contours) (Nitsche et al., 2007) with coastlines and grounding lines from MOA2009 (Haran et al., 2014). The light gray line shows the NBP10-05 cruise track between stations. The numbered black lines (1–4) denote hydrographic sections shown in Figures 4 and 8. Several station locations are circled and referenced by color in Figures 3A and 9A. The one circled in green was also the location of the sediment trap (Figure 2). The Dotson Ice Shelf (DIS) is situated between the Bear Peninsula (BP) and the Martin Peninsula (MP), and the multi-branched Getz Ice Shelf (GIS) is to its east. Location of the study area in the South Pacific sector of west Antarctica in indicated in the upper left inset. Sea ice conditions observed on 2 January 2011 by the Moderate Resolution Imaging Spectroradiometer (MODIS) on the NASA Terra satellite, showing the extent of the Amundsen Sea Polynya (ASP), sampling stations (red dots) and cruise track (blue line), are indicated in the upper right inset. The Thwaites Fast ice and Iceberg Tongue (TFIT) borders the ASP to the east, and to its south (not labeled) is the Thwaites Glacier Tongue.

doi: 10.12952/journal.elementa.000065.f001

2015), which triggers accelerated glacier flow and thinning of the inland ice sheet (Pritchard et al., 2009; Jacobs et al., 2011; Rignot et al., 2014). One goal of the Amundsen Sea Polynya International Research Expedition (ASPIRE) was to determine whether glacial meltwaters could fuel the high primary production observed there (Yager et al., 2012).

Although some atmospheric warming has occurred in the region (Steig et al., 2009; Bromwich et al., 2012), the main source of heat for glacial melting here is thought to be the warm, saline Circumpolar Deep Water (CDW) that originates from the mid-layers of the Antarctic Circumpolar Current (ACC) and is found at depth on the continental shelf in the Amundsen Sea. While the circulation in the ASP region is not well known, there have been attempts to resolve the flow of CDW along the deep down-sloping submarine trough (here referred to as the Dotson Trough) that bisects the continental shelf in the central Amundsen Sea (Figure 1). Via this trough, CDW accesses the continental shelf (Arneborg et al., 2012; Wåhlin et al., 2012, 2013), flows southward towards the coast (Wåhlin et al., 2010; Jacobs et al., 2013) and circulates under the Dotson Ice Shelf (DIS) and the Getz Ice Shelf (GIS) to the west.

When CDW encounters the underside of a floating ice shelf, it induces melting through latent heat transfer, which in turn cools and freshens the CDW (Jenkins, 1999). A geostrophically-driven outflow (Potter et al., 1988; Jenkins et al., 2010; Jacobs et al., 2011; Dutrieux et al., 2014) then delivers melt-laden waters to the ASP region. Some of the CDW-generated meltwaters may come from ice shelves east of the ASP (i.e., Pine Island, Thwaites and Crosson) via a westward-flowing coastal current that combines with the DIS outflow. In the ASP region, the subsurface glacial meltwater from multiple sources is then entrained into the winter mixed layer (WML) every winter during sea ice growth and brine-induced deep mixing. During the ice-free spring and summer, strong wind events or mechanical mixing associated with drifting icebergs might also mix subsurface glacial meltwater into the upper ocean. Deep mixing in the ASP may also be driven by eddies (St-Laurent et al., 2014) and tides (Robertson, 2013). This melt-laden layer, originating from the DIS and other ice shelves upstream of the ASP is also a known source of iron to the ASP (Sherrell et al., 2015).

Our study region in the greater ASP area included the ocean waters in front of the DIS, a ~ 50 km wide ice shelf at its terminus that faces northward between the Bear and Martin Peninsulas (Figure 1). The DIS is a dynamic ice shelf characterized by notches, protruding sections and frequent calving events. The bathymetry in front of the DIS is deepest in the center (> 1000 m) and becomes shallower to the east and west. The deepest portion is part of the Dotson trough system that bisects the continental shelf, branching mid-shelf towards the GIS and DIS (Nitsche et al., 2007). There is known tidal, seasonal and yearly variability in CDW properties found at depth in front of the DIS (Figure 2) (Jacobs et al., 2012). Variability associated with tidal forcing alone may increase basal melting of DIS by up to 52% (as compared to model simulations without

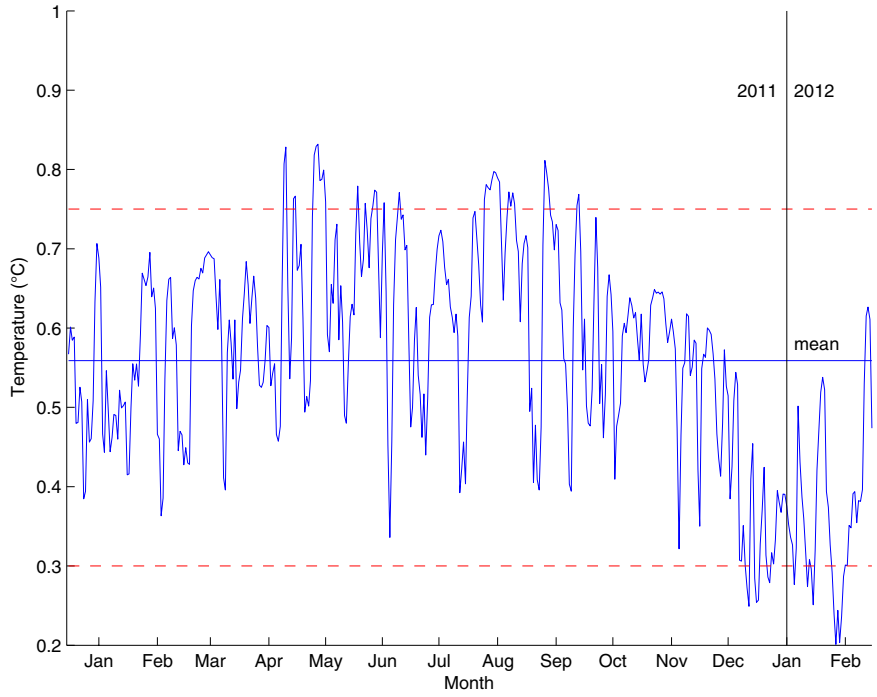

Figure 2

Temperature variability at depth near the Dotson Ice Shelf.

Time series of temperature at 753 m on the sediment trap mooring deployed during ASPIRE on 16 December 2010, retrieved 16 February 2012 (Ducklow et al., 2015). Trap was located at 73.82°S and 113.07°W (bottom depth 785 m). Also shown are the upper and lower temperature ranges observed by the Jacobs mooring (deployed at 74.06°S and 112.42°W during 2006–07, sensor depth 851 m, ranges based on Figure 7 in Jacobs et al., 2012). This time series shows considerable temporal variability, from weekly to seasonal. The latter differs somewhat from the seasonal variability observed at 851 m by the Jacobs mooring in 2006–2007 (the latter showed cooler temperature in ~ March–May and ~ September–October, whereas here cooler temperatures are distinct in December–February).

doi: 10.12952/journal.elementa.000065.f002

tides) (Robertson, 2013). We note that the ASPIRE's sampling program began when near bottom temperatures in front of the DIS were near the average reported for the 1.2-year mooring deployment (Figure 2).

The DIS is estimated to be melting at an average rate of 7.8 m yr^{-1}, while the Pine Island, Thwaites and Crosson ice shelves to the east are melting at 16.2, 17.7 and 11.9 m yr^{-1}, respectively (Rignot et al., 2013). This more rapid melting to the east is partly attributed to a less-modified (i.e. warmer) CDW entering the eastern trough system leading to these other ice shelves (Jacobs et al., 2012), as well as to differences in sub-ice shelf circulation (Jenkins et al., 2010; Joughin and Alley, 2011). The bathymetry of the Dotson trough may also limit the amount of CDW accessing the DIS ice shelf cavity, given the narrowing of the trough north-northeast of Martin Peninsula and the relatively shallower trough depths (Nitsche et al., 2007).

The ASP area is bounded to the east by the Thwaites Fast ice and Iceberg Tongue (TFIT), to the south by the coast (including DIS and GIS), and to the north and west by sea ice (Figure 1 inset). Similar to the Mertz Glacier Polynya (Massom et al., 2001), and other coastal polynyas with fast/land ice barriers to their east (Fraser et al., 2012; Nihashi and Ohshima, 2015), the ASP typifies a barrier coastal polynya. Prevailing southeasterly winds blow over the TFIT to keep the ASP ice-free. The ASP is thus a perennially occurring latent heat polynya (Arrigo et al., 2012), though there may be a sensible component to the polynya heat budget as well (Stammerjohn et al., 2015). A relatively small portion appears to remain ice-free in winter (< 10,000 km^2), but in November it begins to expand, reaching a mean maximum opening in February (> 60,000 km^2), after which it rapidly and consistently closes in March. At its spring–summer extent, the open waters of the ASP cover a wide range of depths, including the shallow bank area north of Bear Peninsula (~ 150–300 m) and the deep trough area (~ 600–1200 m) underlying the central ASP.

Until recently, there was a paucity of data from the ASP area, with attention instead given to the coastal area and/or the outer shelf area (Wåhlin et al., 2010; Arneborg et al., 2012; Jacobs et al., 2012; Wåhlin et al., 2012, 2013). Here, we summarize the first densely-sampled hydrographic survey of the ASP (Randall-Goodwin, 2012), including a detailed assessment of freshwater distributions. We first examine the properties, spatial extent and circulation of water masses in the ASP as observed during ASPIRE. We then analyze the vertical and spatial distributions of meteoric and sea ice melt fractions determined from stable oxygen isotope ($\delta^{18}O$) measurements. These distributions are compared to fractions of subsurface (below the mixed layer) glacial meltwater estimated from profiles of temperature, salinity and dissolved oxygen. We then discuss the relative contributions and delivery of freshwater inputs to the ASP, including the importance of the DIS outflow, its circulation in the ASP, and the role of drifting icebergs ubiquitous in the ASP region in mixing melt-laden CDW up into the mixed layer.

Methods

Collection and sources of data for ASPIRE

An intensive hydrographic, biological and biogeochemical survey of the ASP area was conducted during a 27-day cruise in mid-December 2010 to early January 2011 aboard the RVIB *Nathaniel B. Palmer* (NBP10-05). The cruise track crossed bathymetric gradients and included a high-resolution survey of the DIS front (Figure 1). The ASP hydrographic data comprised 86 conventional Conductivity-Temperature-Depth (CTD) casts, 31 Trace Metal Clean (TMC) CTD casts, and 57 Expendable Bathythermograph (XBT) profiles. At many stations (Figure 1), multiple CTD and TMC casts were acquired, but at every station there was at least one full-depth profile taken within 10 m of the bottom (determined with a Benthos PSA-916 altimeter and a Sea-Bird Electronics (SBE) bottom contact switch with a 10 m line).

The CTD and TMC packages included a SBE 911plus system on 24- and 12-bottle SBE32 rosettes, respectively, each equipped with dual temperature/conductivity sensors and 1 (TMC) or 2 (CTD) SBE43 oxygen sensors. Sensors were calibrated before and after the cruise and post-processed following SBE protocols. All post-cruise corrections were negligible and within the reported accuracy of the SBE temperature and conductivity sensors (0.001°C and 0.0003 S m^{-1}, respectively). During the cruise, CTD salinity measurements were also validated against discrete salinity samples measured on a Guildline Autosal salinometer, while the oxygen sensor data were independently calibrated against discrete samples taken for oxygen titration using the Winkler method (Knap et al., 1996).

Ocean currents were measured with a Teledyne RD Instruments 'Ocean Surveyor' 38-kHz ship (hull-mounted) Acoustic Doppler Current Profiler (SADCP). The SADCP data were calibrated and corrected post-cruise by Eric Firing and Jules Hummon at University of Hawaii. Bathymetry data were acquired by a Simrad EM120 Multibeam system aboard the NBP. This system was also used to estimate the DIS draft during an along-shelf survey. On December 17 from 0900 to 1400 GMT the NBP performed a transect along the DIS front, with the ship maintaining a distance of ~ 200 m from the ice shelf front to record the approximate draft of the DIS, corresponding bathymetry and ocean current and thermal structure (the latter by deploying XBTs every 2–4 km). Underway measurements continuously recorded surface properties, and ice shelf freeboard was determined by several sextant observations. We also acquired 4 TMC and 1 CTD casts at select locations, including the eastern- and western-most locations and over the deepest portion of the central trough.

The Polar Geospatial Center at University of Minnesota and the National Snow and Ice Data Center provided visible, infrared and microwave satellite data. The image data used in this study are from the MODIS (Moderate Resolution Imaging Spectroradiometer) 250 m-resolution instrument on the NASA Terra and Aqua satellites. Those data, when cloud-free, provided excellent sea ice coverage, polynya boundaries, and locations of icebergs.

Collection and analysis of oxygen isotope samples

Samples for $\delta^{18}O$ analysis were drawn from CTD Niskin bottles into 20-mL glass scintillation vials with poly-seal cone liner caps that were sealed further with vinyl electrical tape. A total of 384 samples were drawn from 44 CTD casts acquired at 35 stations. (Sample depths and station locations are presented as part of the analyses under Results.) Typically 6-12 depths were sampled from each cast. The samples were boxed and kept cool during transport from Antarctica to the U.S., where they were analyzed at the Department of Earth and Planetary Sciences, Rutgers University.

At Rutgers University, the $H_2{}^{18}O/H_2{}^{16}O$ ratio measurements were made on a FISONS OPTIMA Mass Spectrometer equipped with a MicroMass Multiprep automatic sample processing system after water sample equilibration with CO_2 using standard methods (Epstein and Mayeda, 1953; Fairbanks, 1982). Oxygen isotope ratios are reported as the per mil (‰) deviation of the $^{18}O/^{16}O$ ratio of the sample from that of Vienna Standard Mean Ocean Water (VSMOW) (Coplen, 1994). Precision is estimated to be ±0.034‰ (1 SD) as determined by multiple (n = 12) daily analyses of a laboratory standard. All samples were run in duplicate and replicates were required to measure within 0.068‰ to be included in the finalized data set. Instrument linearity and accuracy were determined by comparison of the laboratory standard to NIST reference standards: VSMOW, GISP, and SLAP. The $\delta^{18}O$ depth-discrete data were then plotted to visually inspect for obvious outliers (i.e., any values lying well outside the range described by all of the $\delta^{18}O$ data), which resulted in the identification of 6 individual outliers from 6 different depths in 5 different CTD casts. There were no anomalous departures in the sensor or bottle data associated with these 6 anomalous $\delta^{18}O$ values, thus we suspected that theses $\delta^{18}O$ samples must have been contaminated. These six values were removed from further analysis.

Determination of meteoric and sea ice melt fractions

The primary aim of this paper is to characterize the freshwater inputs that create the stratified water column found within the ASP region. In this context, it is possible to quantify the overall freshwater prevalence at any point by simple comparison of its measured salinity with that of the oceanic source water, i.e., the

regional CDW. However, this approach does not provide information on the source of the freshwater added; to elucidate sources, additional tracers are required.

For the ASP region, the freshwater sources include meteoric water, i.e., freshwater inputs derived from the atmosphere. These inputs can be delivered as direct precipitation to the ocean, as snow falling onto sea ice that later melts, or as snow that accumulates to form ice sheets and ice shelves, ultimately to be injected into the ocean as glacial discharge. Additionally, within the active ASP, sea ice growth and decay seasonally redistribute freshwater vertically (either by mixing down surface sources of freshwater via brine rejection during sea ice growth in autumn–winter or by retaining freshwater sources in shallow surface layers during spring-summer sea ice melt). The advection of sea ice into or out of an area can also lead to net increases or decreases of sea ice melt, respectively. Finally, the presence of seasonal sea ice modulates the injection of meteoric water to the ocean when sea ice melts each spring. These are the processes that we quantify herein.

We focused initially on partitioning the net freshwater balance between the total inputs from all meteoric sources (precipitation and glacial discharge in the form of melting ice shelves and icebergs) and the input/extraction due to sea ice melt/formation. Following Meredith et al. (2008, 2010, 2013), we used a three-endmember mass balance approach (Equation 1) (Östlund and Hut, 1984), employing salinity and $\delta^{18}O$ as tracers. This approach assumes that the observed salinity and $\delta^{18}O$ values in the water column have resulted from a mixture of sea ice melt, meteoric inputs and CDW, all three of which have well-separated salinity and $\delta^{18}O$ values in pure form.

$$\begin{aligned} f_{sim} + f_{met} + f_{cdw} &= 1 \\ f_{sim}{}^{*}\, S_{sim} + f_{met}{}^{*}\, S_{met} + f_{cdw}{}^{*}\, S_{cdw} &= S_{obs} \\ f_{sim}{}^{*}\, \delta_{sim} + f_{met}{}^{*}\, \delta_{met} + f_{cdw}{}^{*}\, \delta_{cdw} &= \delta_{obs} \end{aligned} \quad (1)$$

In this set of three equations and three unknowns, f is the fraction of the freshwater components in pure form, denoted by subscripts for sea ice melt (sim), meteoric water (met), and cdw, while subscripted S and δ are the salinity and $\delta^{18}O$ values of the same three components in pure form. The quantities S_{obs} and δ_{obs} on the right-hand side are the observed values of salinity and $\delta^{18}O$ in each water sample.

We assigned values of 34.62 and –0.059‰ for the CDW salinity and $\delta^{18}O$ endmember, respectively, based on our observations of CDW in the Dotson trough (Figure 3A). For sea ice, we used values of 7 and 2.1‰ for salinity and $\delta^{18}O$, respectively. This choice was based on our own unpublished observations of salinity and $\delta^{18}O$ measurements in sea ice from a previous expedition to the Amundsen Sea (January–February 2009); these values are also consistent with Fransson et al. (2011) and Meredith et al. (2013). Given known variability in CDW properties at depth in the Dotson trough (Jacobs et al., 2012) and in age/thickness of sea ice, these endmember values will vary seasonally and yearly. However, as discussed below, the uncertainty in the meteoric endmember is much greater, and will thus dominate the uncertainty in our freshwater fractions.

For the meteoric endmember, we assigned values of 0 and –25‰ for salinity and $\delta^{18}O$, respectively. This choice was based on the distribution of our data in $\delta^{18}O$-salinity space (shown and discussed below). However, as discussed by Meredith et al. (2008, 2010, 2013), the greatest uncertainty in this estimate lies in the $\delta^{18}O$ meteoric endmember (whereas the endmembers for CDW and sea ice are relatively well-constrained by observation). We therefore bracketed our results using $\delta^{18}O$ endmembers of –20‰ and –30‰ (i.e., ±5‰) based on values previously reported for the southern Bellingshausen Sea (Jenkins and Jacobs, 2008) and eastern Amundsen Sea (Hellmer et al., 1998; Jenkins, 1999), respectively. Given this range in the $\delta^{18}O$ endmember, the uncertainty in the derived meteoric and sea ice melt percentages (which includes uncertainty in measurement error), is no more than ±0.5%.

Once meteoric and sea ice melt fractions were determined, column inventories were computed based on vertical interpolations of the $\delta^{18}O$ depth-discrete profiles. Various interpolations were tested, including a shape-preserving piecewise cubic spline, but we elected to use a simple linear interpolation as it yielded the most conservative estimate. Before performing the interpolation, some $\delta^{18}O$ profiles had to be amended as follows. For those few casts where samples were not drawn from the near surface bottle, a surface value was assigned that matched the next sampled depth (i.e., within the surface mixed layer). There also were a few casts where the bottom bottle was not sampled; in those cases, a very conservative value of zero was assigned for $\delta^{18}O$ of the bottom depth. Uncertainty in the column inventories resulting from the uncertainty in the freshwater percentages was approximately ±2 m.

We note that the choice of representative "regional" properties for the CDW and other endmembers in our analyses is a subjective one that influences our results. For example, choosing on-shelf CDW properties for the endmember means that saltier waters found on the continental slope will have a negative freshwater fraction. However, our main interest is in the ASP region, so we focused on the freshwater inputs that create the observed stratification in that region, noting that there will be contributions both from local freshwater inputs and from the transport of waters with a non-zero freshwater fraction into the region as well.

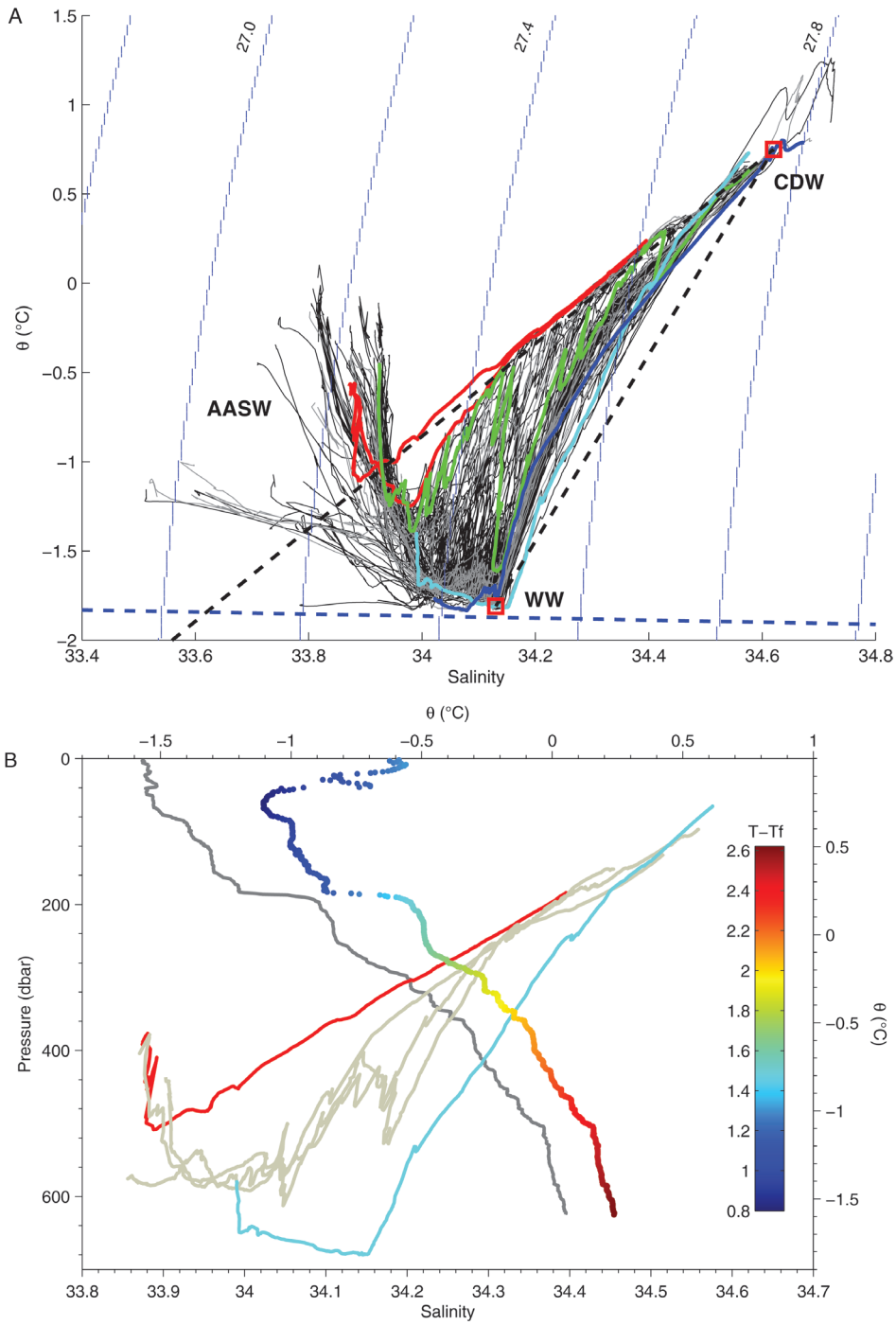

Figure 3

Water mass properties and mixing lines.

(A) Property-property plot of θ-S of all CTD data (black, conventional CTD; gray, trace-metal clean CTD), with five casts highlighted: red, Dotson Ice Shelf (DIS) outflow Stations 60 (top red line) and Station 61 (bottom red line); green, iceberg/mixing Station 57.26; blue, shelf break Station 4; and cyan, GIS Station 5. Water mass types include: Antarctic Surface Water (AASW), Winter Water (WW) and Circumpolar Deep Water (CDW). Blue dotted line indicates the surface freezing temperature; black dotted lines show the meltwater-CDW and the WW-CDW mixing lines. The red squares indicate the canonical WW and CDW values. Lines of constant density (σ_θ) are also shown. (See Figure 1 for locations of highlighted casts, matched by color.) (B) Details of θ and salinity observed in front of the DIS. The vertical profiles are from the DIS outflow Station 60, with θ shaded by degrees above freezing. In θ-S space, the upper red line is the DIS outflow Station 60, the gray lines are the other 3 DIS Stations 9, 10, and 11. The lower cyan line is from GIS Station 5, added for reference.

doi: 10.12952/journal.elementa.000065.f003

Determination of subsurface glacial meltwater fractions

Having quantified the freshwater inputs due to meteoric water and sea ice processes, we next sought to distinguish meteoric inputs from subsurface melting of glacial ice, as these deep inputs to CDW result in buoyancy gain and can drive upwelling or formation of a melt-laden CDW layer available to deep mixing. Because subsurface glacial melt is a meteoric input, $\delta^{18}O$ cannot be used to distinguish it from surface-derived meteoric inputs. For example, isotopic values in local precipitation and ice shelf melt are similar, unless the

interior parts of the catchment basin for the ice shelf are remote from the coast and at high elevation, which they are not in the case of DIS. However, subsurface inputs of glacial meltwater can be distinguished from other freshwater sources by their low potential temperature (because the latent heat of fusion is extracted from the ocean) and high dissolved oxygen concentration (because all the air trapped in the ice goes into solution).

To calculate glacial meltwater fractions below the wind-mixed layer, Jenkins (1999) used a similar approach to that in the previous section, but here we are using potential temperature, salinity and dissolved oxygen as tracers, and CDW, Winter Water (WW) and glacial meltwater as endmembers. Using WW as an endmember effectively excludes those surface inputs of freshwater that create the WW properties, so the results of these calculations should be seen as the component of the total meteoric water input that has come from deep melting and upwelling versus that derived from surface input and convective mixing beneath growing sea ice. The use of three tracers with three endmembers can be solved algebraically in a number of ways. Jenkins (1999) used three separate estimates of meltwater fraction based on the three possible tracer pairs, and formulated the algebraic solution to the equivalent of Equation (1) as a conservation equation for a composite tracer defined by:

$$\psi_{obs}^{2,1} = (\chi^2 - \chi^2_{cdw}) - (\chi^1 - \chi^1_{cdw}) * (\chi^2_{ww} - \chi^2_{cdw})/(\chi^1_{ww} - \chi^1_{cdw}) \quad (2)$$

The χ denotes a CTD sensor observation at each depth, and superscripts 1 and 2 represent the conservative tracers (potential temperature, salinity, or dissolved oxygen); the subscripts, as before, denote water masses WW and CDW. The subsurface glacial meltwater fraction is then calculated by

$$f_{gmw} = \psi_{obs}^{2,1} / \psi^{2,1}_{gmw} \quad (3)$$

The numerator in Equation (3) is the composite tracer observed at each depth of the CTD cast, while the denominator is the value for pure glacial meltwater (gmw), where we used −89°C, 0 and 25.9 mL L^{-1} for potential temperature, salinity and dissolved oxygen, respectively, based on previous studies in the Amundsen Sea (Jenkins, 1999; Jacobs et al., 2011) and on the extrapolation of mixing lines in property-property space. The composite tracer values for CDW (0.75°C, 34.62, 4.52 mL L^{-1}) and WW (−1.81°C, 34.13 and 6.49 mL L^{-1}) for potential temperature, salinity and dissolved oxygen, respectively, were identified from observation as "core" properties of the warmest, saltiest water mass in the deep trough on the shelf and the coldest, saltiest water mass in the winter mixed layer, respectively (Figure 3A). For additional details on the fundamentals of mixing and endmember choices within the context of ocean-ice shelf interactions in the Amundsen Sea, see Jenkins (1999) and references therein.

In our profile plots of glacial meltwater fraction, we considered results from all three composite tracers (i.e., O_2-θ, O_2-S and θ-S; see Results). Below the wind-mixed layer (distinct from and shallower than the WML), the three composite tracers agreed well, but in the wind-mixed layer they became non-conservative. There the curves for O_2-θ and θ-S diverged rapidly from each other due to the impact of interactions with the atmosphere on all tracers. For this study, the depth of surface influence was identified as the level where O_2-θ and θ-S deviated more than 8‰ in glacial meltwater fraction, and values shallower than that level were ignored.

As discussed by Jenkins and Jacobs (2008), the uncertainty in the glacial meltwater fractions derives from the uncertainty in defining linear trends associated with mixing in the main pycnocline and between CDW and a meltwater source that is assumed to be uniform. The assumption of linearity completely breaks down in the surface mixed layer, where temperature and dissolved oxygen signals are influenced by equilibration with the overlying atmosphere, so these values were ignored. Below this level the main source of error in the calculation is the deviation from the assumed linear trend between CDW and WW properties (Figure 3A), which introduces a bias of up to 5‰ (i.e., 0.5%). It is possible that the curvature is a result of sub-surface meltwater addition, but it is also possible that some is an artifact introduced by the spatial and temporal variability in the properties of the WW that is incorporated into the thermocline. Therefore, precise error estimates are difficult to provide, but we expect them to be of order 0.5% or less.

Results

Regional hydrography and ocean circulation

Water mass structure

In the ASP, there are two primary water masses: warm, saline CDW at depth and an overlying deep layer of cold, relatively less saline winter water (WW) (Figures 3A and 4). During spring–summer, there is also a relatively thin surface layer of Antarctic Surface Water (AASW). This summer surface layer is essentially WW that has warmed and freshened to varying degrees by insolation and seasonal ice melt.

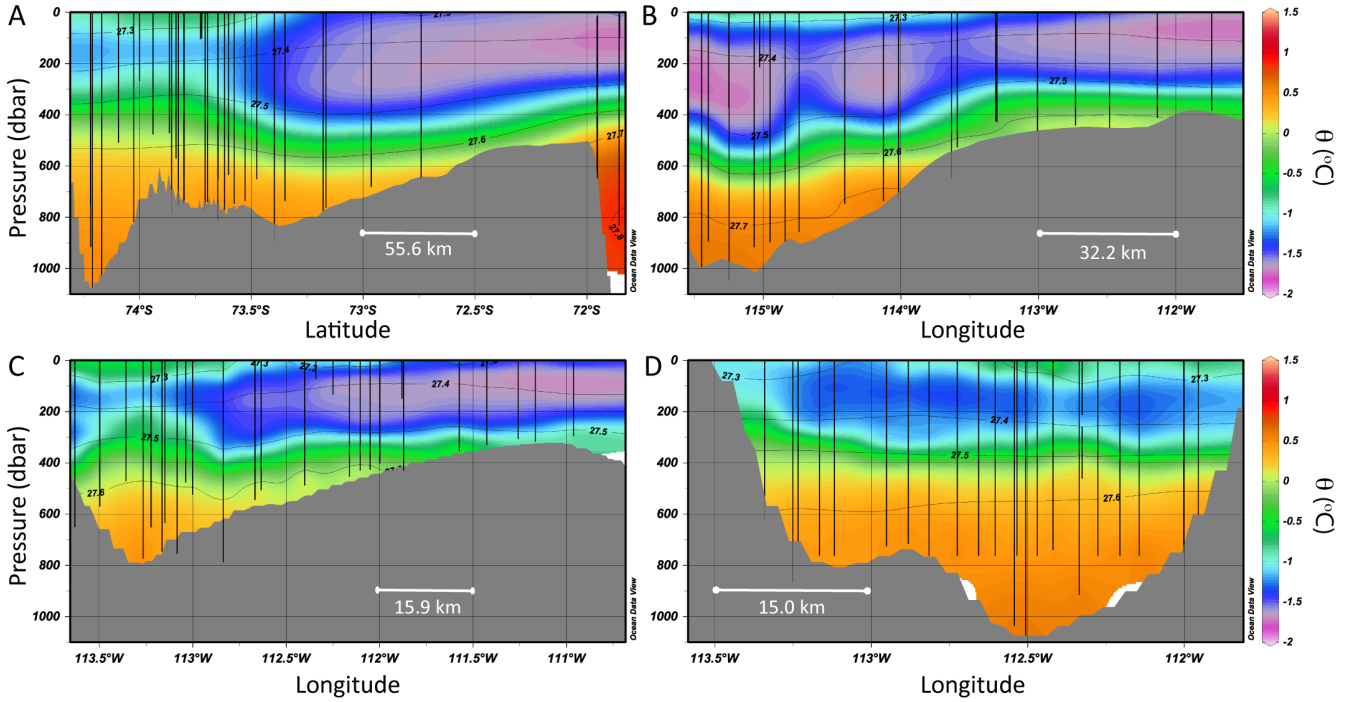

Hydrographic sections of temperature (shading) and density (contoured), south–north along the Dotson trough (Figure 4A) and crossing the trough west-to-east (Figure 4 B– D), revealed the spatial distributions of AASW, WW and CDW in the ASP region observed during ASPIRE. Relative to offshore (Figure 4A, right) CDW on the shelf was cooler and fresher (Figure 4A, left). Nonetheless, within the trough at depth, CDW was still more than 2 degrees above freezing when it reached the DIS (Figure 3B).

The base of the WML, here defined by the ~ 27.5 kg m^{-3} isopycnal, was deep, ranging from ~ 300 m in shallow waters to greater than 400 m over the deep trough. In the southern trough area (south of ~ 73.5°S), the WML attenuated (shoaled and warmed) (Figure 4 A, C, left) due to strong vertical mixing, detected both in front of the DIS and in the vicinity of a drifting iceberg (detailed below). South of ~ 73.25°S a thin layer of AASW corresponded to the open waters of the ASP (Figure 1, inset).

Mixing lines between water masses were identified in potential temperature-salinity (θ-S) space (Figure 3A). Mixing between CDW and WW and between CDW and glacial meltwater (Jenkins, 1999) illustrate the degree of CDW modification observed in the ASP region. For the ASPIRE data, the meltwater-CDW mixing line was an extrapolation from the observed θ-S value for CDW (as observed at depth in the Dotson trough) to the θ-S value for glacial meltwater (–89°C and 0, respectively), taking into account the latent heat of fusion of the ice (Jenkins, 1999). This extrapolation yielded a slope of 2.59, similar to other slope values reported for the Amundsen Sea (e.g., Jacobs et al., 2011). The meltwater-CDW mixing line is used here to provide a visual reference for detecting subsurface glacial meltwater presence.

When viewed in θ-S space (Figure 3A), all of the ASPIRE profiles approached the CDW-meltwater mixing line (upper dotted line) at depth. In contrast, there is a general lack of data on the CDW-WW mixing line, which is due to the fact that few ASPIRE observations represent mixtures of core CDW and WW properties (as defined earlier in the previous section). Instead, the range of observations to the left of the CDW-WW mixing line reveals varying mixtures of modified versions of CDW and WW (e.g., cooler, less salty CDW mixing with warmer, less salty WW) in addition to some amount of subsurface glacial meltwater. The profile highlighted in dark blue, acquired at the shelf break (Station 4), smoothly deviated from the CDW-meltwater mixing line at depth to the CDW-WW mixing line at mid-depths. The profile acquired in front of the GIS (Station 5, cyan) was similar, though with less bending towards the CDW-meltwater mixing line at mid-depths. Most of the other ASPIRE profiles showed layered-like deviations extending towards the CDW-meltwater mixing line at mid-depths, similar to the profile highlighted in green (discussed below).

The two profiles highlighted in red (in Figure 3) are Station 60 (upper red line) and 61 (lower red line). The profile from Station 60 (red circle in Figure 1) closely follows the CDW-meltwater mixing line and was located at the western end of the DIS (just west of Station 10) in 635 m of water and in an area of strong outflow (detailed below). Station 61 (second red circle just north of Station 60 in Figure 1) was north of the outflow area in somewhat shallower waters (520 m); it too showed melt-laden CDW, more so at depth, with less upwelling near the surface (as otherwise indicated by the linear θ-S profile for Station 60). The other profiles in front of the DIS, east of the outflow, also showed melt-laden CDW at depth, as well as deviations

Figure 4

Regional ocean characteristics.

Vertical sections of θ (shading) overlain by σ_θ (black contours) for (A) Section 1, extending south (left) to north (right) from the Dotson Ice Shelf (DIS) front to just offshore of the shelf break along the Dotson trough; (B) Section 2, extending west (left) to east (right) from the Dotson trough (mid-shelf) onto the shallow bank north of Bear Peninsula; (C) Section 3, extending west (left) to east (right) south of Section 2; and (D) Section 4, extending west (left) to east (right) ~ 200 m in front of the DIS. (See Figure 1 for section locations.) The black vertical lines indicate the locations and depths of the CTD profiles.

doi: 10.12952/journal.elementa.000065.f004

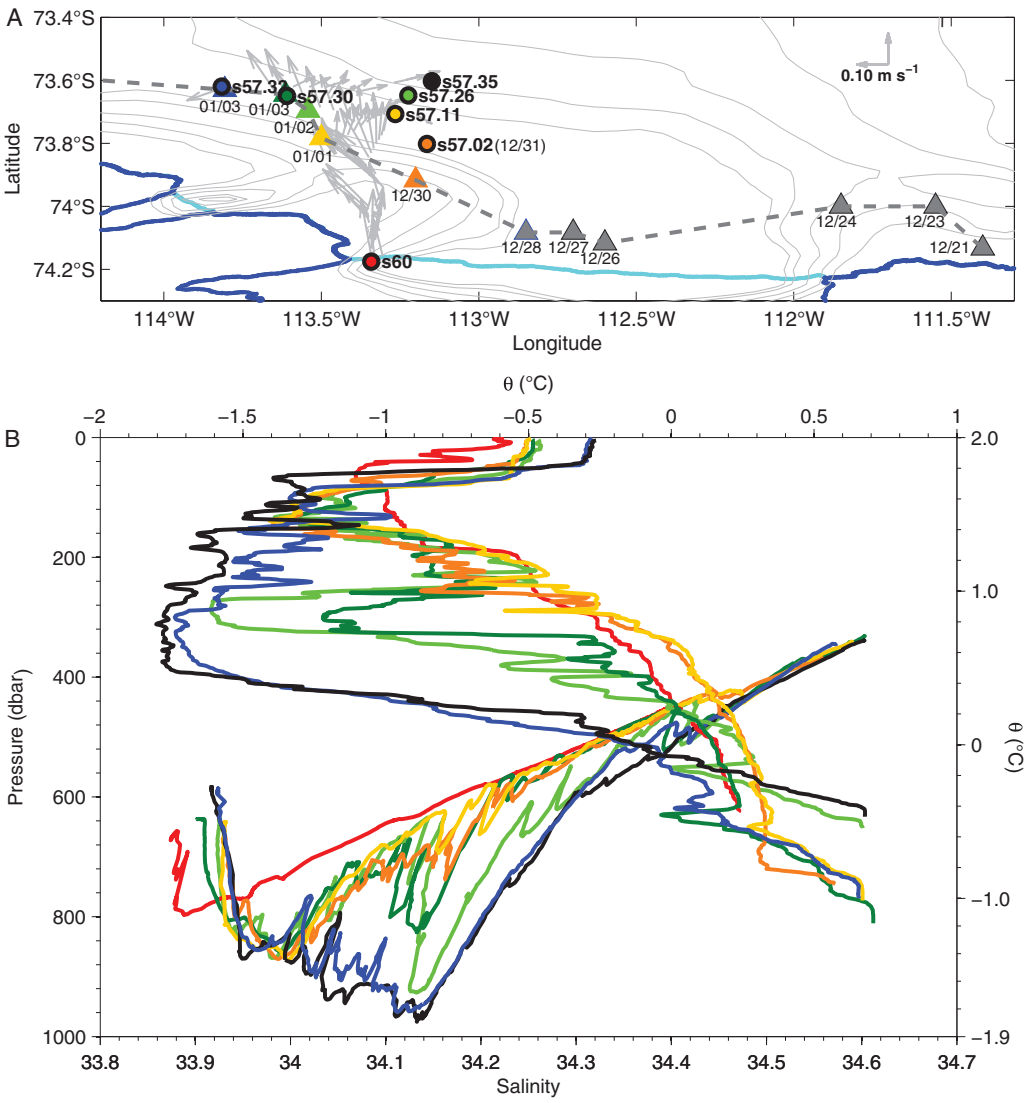

Figure 5

Iceberg drift track and mixing of temperature and salinity.

(A) Iceberg locations (filled triangles) and drift track (dark gray dashed line) shown in relation to CTD casts acquired during Station 57, with Station 60 (DIS outflow, red) added for reference. Iceberg locations were determined from MODIS Terra and Aqua imagery and are dark gray prior to 30 December and then color-matched to the s57 CTD cast acquired closest in space/time (i.e., same day except s57.02), noting that the locations of s57.30 and s57.32 were only ~ 1 km south and north of the drifting iceberg, respectively. Light gray vectors show mean (31-423 m) ocean currents (m s^{-1}) observed between 30 December and 3 January acquired along the NBP10-05 cruise track between 113.2°W and 113.8°W. Bathymetry is from Nitsche et al. (2007); coastlines are from MOA2004 (Haran et al., 2013). (B) Details of θ and salinity observed at the same stations shown in (A), color-matched by location. Waters not mixed by the drifting iceberg were captured at Station 57.32 (blue) and 57.35 (black).

doi: 10.12952/journal.elementa.000065.f005

extending towards the CDW-meltwater mixing line at mid-depths (Figure 3B), similar to the highlighted profile in green (Figure 3A), the latter acquired at Station 57.26 (green circle in Figure 1; Figure 5A).

Station 57 was designated the 'iceberg station' and was located approximately 30 km north of the DIS within the 700 m isobath of the deep trough. The trajectory of the iceberg was from the southeast to the northwest over the locations occupied by Station 57 (Figure 5A). The estimated drift speed was ~ 0.3 knots under light southerly winds. The iceberg was quasi-tabular, ~ 3 km long by ~ 1 km wide, with an irregular freeboard range of 37–50 m (determined by sextant) and an estimated keel depth range of 340–450 m (based on isostasy).

At Station 57, several CTD casts were taken in the vicinity of the drifting iceberg over a period of ~ 2.5 days, both downstream and upstream of its drift trajectory, i.e., in waters perturbed and undisturbed by the drift of the deep-keeled iceberg. Profiles taken in the perturbed waters downstream and closest to the iceberg were similar (e.g., profiles from s57.26 and s57.30 in green and dark green, respectively; Figure 5B), while profiles taken in the undisturbed waters upstream or away from the iceberg (e.g., profiles from s57.32 and s57.35 in blue and black, respectively) showed no deviations in meltwater loading.

Ocean currents and thermal anomalies

Depth-averaged (31–423 m) ocean currents acquired underway (Figure 6) revealed the dominant flow direction as observed during our occupation of the ASP region. We later show a subset of velocity depth profiles, but here our intent is to show the dominant flow directions over the upper ~ 400 m where variability in the vertical was relatively low (< 3 cm s^{-1} SD). In particular, there was a strong northward flow (> 20 cm s^{-1})

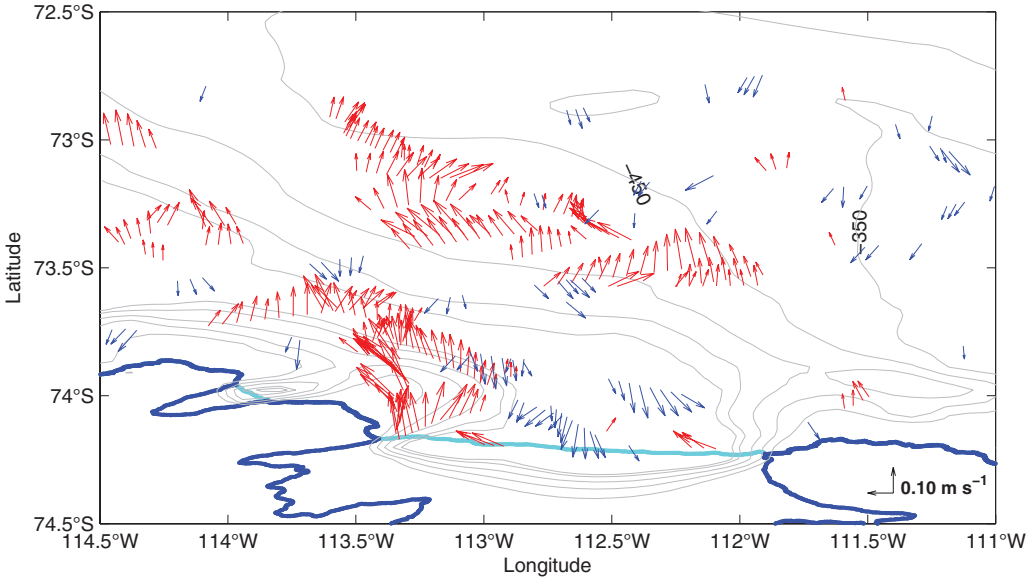

Figure 6

Regional ocean currents observed during ASPIRE.

Vertically-averaged (31–423 m) ocean currents (m s^{-1}) observed underway along the NBP10-05 cruise track, zoomed-in on the central ASP and DIS area. Only velocities greater than ±0.05 m s^{-1} are shown for every 1 km of cruise track. Northward currents are in red colors, southward currents are in blues. Bathymetry is from Nitsche et al. (2007); coastlines are from MOA2004 (Haran et al., 2013).

doi: 10.12952/journal.elementa.000065.f006

north of the DIS outflow and extending north along the western bank of the deep trough. There were other areas of strong northward flow further north and to the east, as well as a few areas of strong southward flow. The SADCP data were not de-tided, and we only show those depth-averaged currents (tidal or non-tidal) greater than 5 cm s^{-1} for clarity. It is certain that some of the flows shown here (Figure 6) contained shear, were tidally amplified and/or generated by transient eddies, all of which are important factors in terms of mixing and melting (e.g., Robertson, 2013). In terms of current direction, however, many locations had overlapping cruise tracks separated in time, and several (though not all) of those revisited locations showed similar directions, most notably the strong outflow area in front of the DIS and the northward flows observed during the crossings onto/off the shallow bank to the northeast of the DIS.

A more detailed examination of ocean currents just north of the DIS (Figure 7A) showed strong northward and southward flows (> 10 cm s^{-1}) concentrated at the western and eastern boundaries of the ice shelf front, respectively, while weaker north-south currents were observed elsewhere along the front. (Here we did not exclude the weaker currents, but we did smooth with a 3-point running mean.) The strong southward (inflow) current of 10–20 cm s^{-1} observed at the far eastern boundary was concentrated at depths below ~ 400 m (and likely extended beyond the SADCP depths of 500–600 m). In contrast, the strong northward (outflow) current observed at the far western boundary was considerably shallower and stronger (> 20 cm s^{-1}) between ~ 100 and 400 m. We estimated the magnitude of the outflow by multiplying its mean (northward) flow (~ 0.20 m s^{-1}) by its estimated depth/width (300 m deep by 2760 m wide) (e.g., based on Figure 7A) and arrived at ~ 0.17 Sv (or 0.17 x 10^6 m^3 s^{-1}). The width of the outflow may actually be greater towards the west, but unchartered (and shallow) waters prevented us from venturing further in that direction.

The current structure in the outflow area of the DIS compared well with its thermal structure (Figure 7B), the latter acquired from 17 XBTs spaced every 2–4 km. There was a distinct shoaling of the thermocline (black contour representing the −1°C isotherm) in the outflow area, corresponding also to a thinning of the ice shelf towards the western end (as estimated from multibeam data). The observed temperature anomalies (temperature at a given depth minus a depth-mean temperature) showed a warm thermal anomaly in the same depth interval where the strongest outflow was observed. The temperature of the outflow waters was ~ 1.0–1.5°C warmer than the in-situ freezing point and consisted of melt-laden CDW as indicated by its profile in θ-S space (Figure 3B) and its meltwater content (shown and discussed below).

Freshwater distributions

Regional oxygen isotope values

Reflecting the contribution from the meteoric endmember (−25‰) relative to the endmembers for CDW (−0.059‰) and sea ice (2.1‰), the lowest $\delta^{18}O$ values (< −0.6‰) were found in thin surface layers over the deep trough and south towards the DIS (Figure 8), suggesting local surface freshwater inputs from the TFIT and DIS and the import of surface freshwater from further east, upstream of the DIS (e.g., the Pine Island Bay area). The surface freshwater inputs come from solar-warmed waters inducing surface melt of icebergs, ice shelves and other sources of precipitation (snow on sea ice).

Low values of $\delta^{18}O$ (−0.4 to −0.6‰) were also observed throughout the deep winter mixed layers, indicating redistribution of meteoric surface inputs and/or contributions from deep melting and upwelling

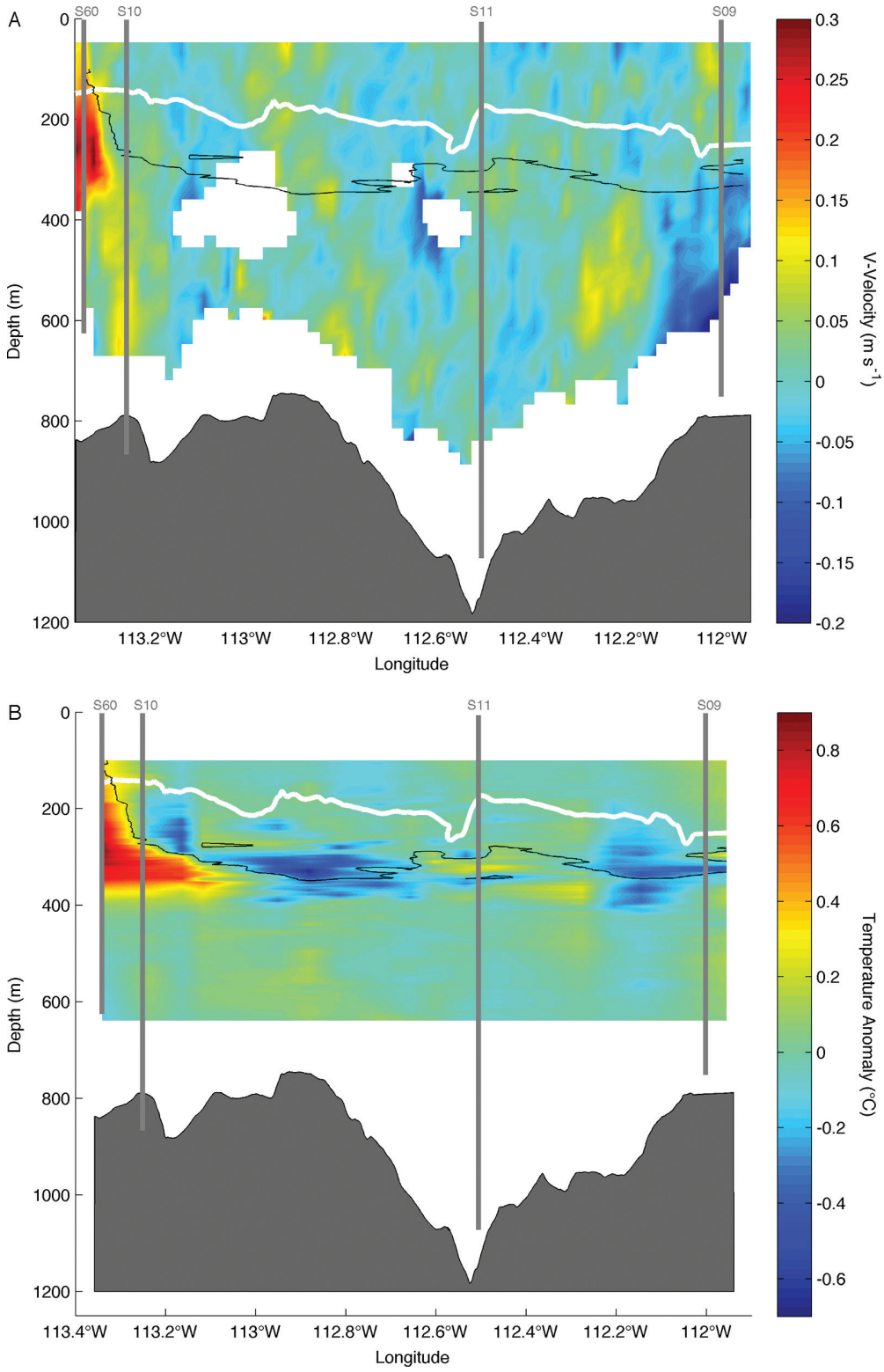

Figure 7

Ocean currents and temperature anomalies in front of the Dotson Ice Shelf.

(A) North–south (positive–negative) ocean currents (m s^{-1}) observed ~ 200 m in front of the DIS acquired underway during a transect along the ice shelf front. Station locations and depth of TMC CTDs are indicated by the gray vertical lines. White areas indicate no SADCP data. Velocities were smoothed by a running mean, effectively removing velocities less than ±0.05 cm s^{-1}. (B) Temperature anomalies (temperature at a given depth minus a depth-mean temperature) from XBT data acquired during the same transect. In both plots, the white contour is a multibeam estimate of the ice shelf draft, and the black contour is the −1.0 °C isotherm. Bathymetry is from Nitsche et al. (2007).

doi: 10.12952/journal.elementa.000065.f007

(e.g., CDW inducing basal ice shelf melt or the melt of deep iceberg keels). In contrast, the highest $\delta^{18}O$ values were found at depth offshore of the shelf break (> −0.02‰), reflecting an isotopically heavier CDW off the shelf than on the shelf. CDW on the shelf is made relatively lighter (< −0.1‰) primarily by mixing with overlying isotopically lighter waters. In front of the DIS (Figure 8D) there was a shoaling of the $\delta^{18}O$ values to the west (left) in the outflow area, consistent with the shoaling of isotherms (Figures 4D and 7B) caused by the upwelling of CDW and its relatively heavier isotopic content.

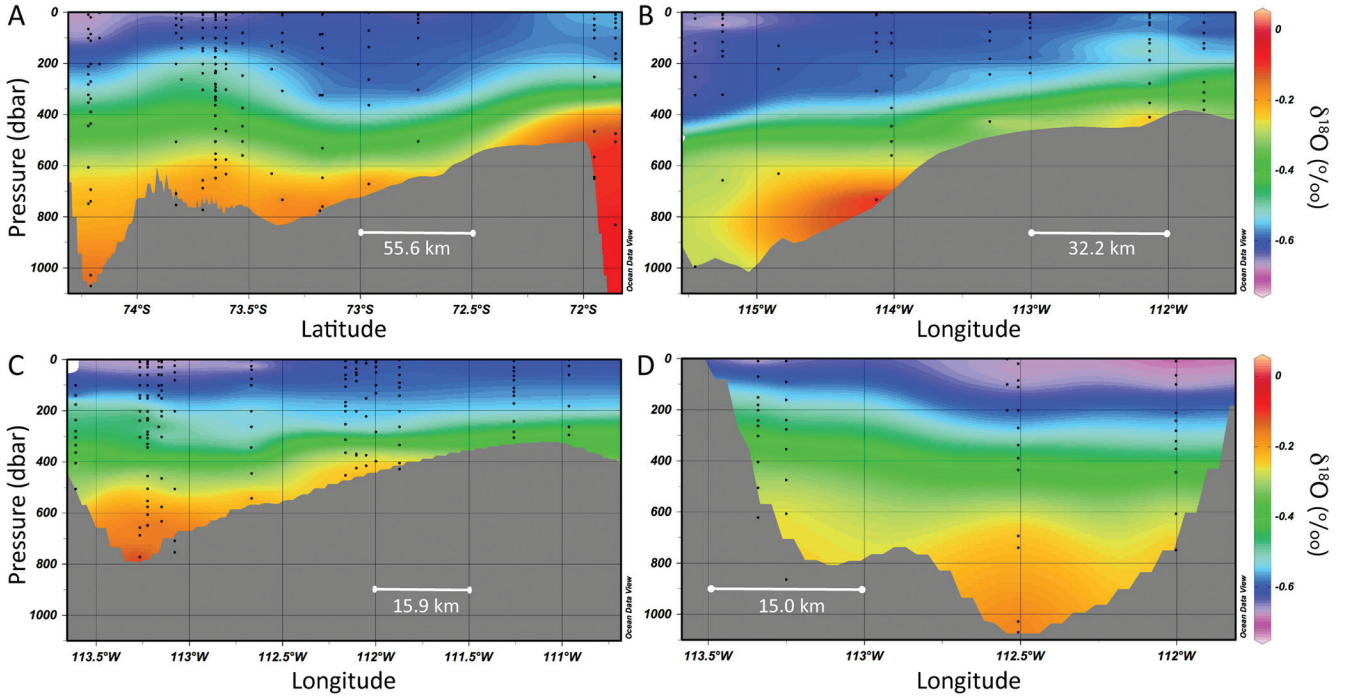

The individual $\delta^{18}O$ profiles (Figure 9A) showed more clearly the range of $\delta^{18}O$ values in the mixed layer versus at depth. Station 4 at the shelf break (Figure 9A, dark blue) showed the relatively heavier isotope values both at the surface and at depth. The other two profiles with similar isotopically heavier deep values were also from the shelf break (another cast from Station 4 and one from Station 68). The two profiles from in front of the DIS (Figure 9A, red) illustrated the varying inputs of meltwater there. The outflow station (Station 60; Figure 9A, red-filled circle) clearly showed heavier isotope values near the surface (~ 100 m) compared to $\delta^{18}O$ values observed at that depth east of the outflow (Figure 8D), the former caused by the upwelling of melt-laden CDW. This profile stands in contrast to the cast acquired at the mid-ice-shelf location (Station 11; Figure 9A, red plus symbol), which showed much lighter isotopic values throughout its mixed layer. The profile near the GIS (Station 5; Figure 9A, cyan) also showed lighter isotopic values throughout its mixed layer. The cast from the iceberg station (Station 57.26; Figure 9A, green) showed a deviation towards heavier isotopic water at ~ 200 m, where mixing by the iceberg caused entrainment of CDW, consistent with the deviations detected in θ-S space (Figures 3A and 5B).

When plotted in $\delta^{18}O$-S space (Figure 9B), many of the surface (light gray) and mixed layer (dark gray) values deviated from the meteoric-CDW mixing line (bold diagonal). Deviations left or right of the meteoric-CDW mixing line are due to net sea ice melt (freshening) or formation (salinification), respectively. Surface values showing net sea ice melt tended to be from locations near or in the sea ice bordering the polynya to the north, i.e., not to the south where sea ice production is most active due to persistent cold southerly winds that create conditions favorable for new ice formation and northward advection. Consequently, in the northern area of the polynya there is an influx of sea ice from the south, which contributed to either less net freezing or net sea ice melt (as indicated by the surface values to the left of the meteoric-CDW mixing line). In contrast, surface samples from the southern polynya indicated net sea ice formation, as do most of the winter mixed layer values, consistent with this area being an active latent heat polynya under the influence of persistent southeasterly winds throughout the year. Details of these regional distributions are discussed below.

Fractions of meteoric, sea ice melt and subsurface glacial meltwater

Vertical profiles of freshwater fractions (Figure 10, meteoric in blue, sea ice melt in red) and fractions of subsurface glacial meltwater (Figure 10, in black) reflect variability in freshwater content across four representative areas: the DIS front (Figure 10 A–D), the iceberg area (Figure 10 E–H), the outer deep trough area (Figure 10 I–L), and the shallow eastern bank area (Figure 10 M–P). (These geographic locations are marked on Figure 11A and 12A; note different seafloor depths.) We first discuss the three different fractions separately.

Meteoric fractions showed relatively large values in the WML (> 15‰ or 1.5%), with the greatest accumulations in the deep trough areas where WMLs were deepest (e.g., Figures 10 B–D, H–K). In those locations, water column inventories of meteoric content (precipitation and glacial melt) ranged from 11 to 13 m. Even over the shallow bank area (Figure 10 M–P), meteoric fractions in the WML were as high as

Figure 8

Regional oxygen isotope values.

Vertical sections of discrete $\delta^{18}O$ for the same sections shown in Figure 4: (A) Section 1, extending south (left) to north (right) from the DIS front to just offshore of the shelf break along the Dotson trough; (B) Section 2, extending west (left) to east (right) from the Dotson trough (mid-shelf) onto the shallow bank north of Bear Peninsula; (C) Section 3, extending west (left) to east (right) south of Section 2; and (D) Section 4, extending west (left) to east (right) ~ 200 m in front of the DIS. (See Figure 1 for section locations.) The black dots indicate the locations and depths of the discrete bottle samples.

doi: 10.12952/journal.elementa.000065.f008

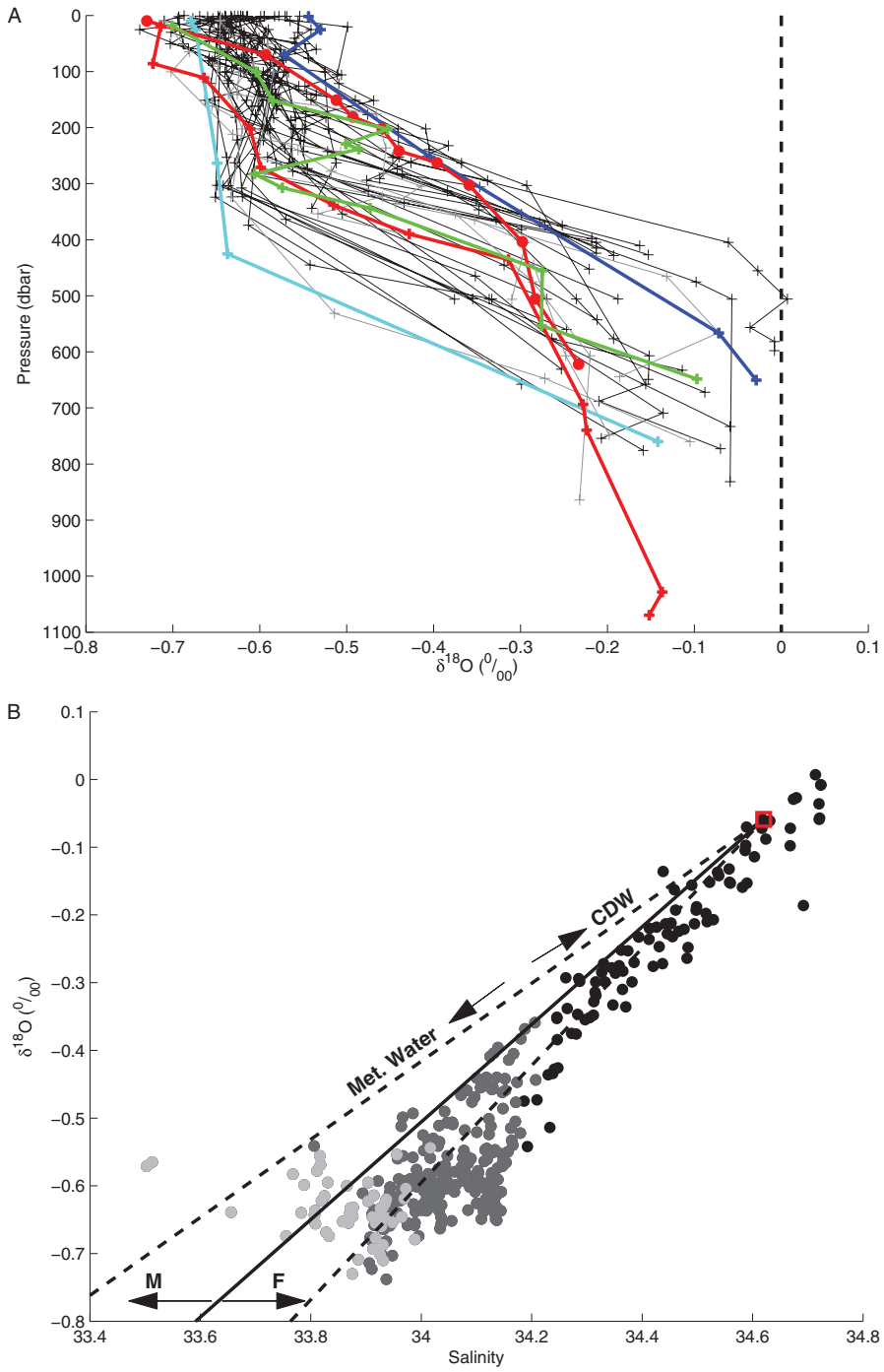

Figure 9

Oxygen isotope vertical distributions and mixing lines.

(A) Vertical profiles of discrete $\delta^{18}O$ concentrations with five casts highlighted: blue/+, shelf break Station 4; red/+, DIS deep Station 11; red/filled circle, DIS outflow Station 60; green/+, iceberg/mixing Station 57.26; and cyan/+, GIS Station 5. (See Figure 1 for locations of highlighted casts, matched by color.) The zero vertical line is added for reference. (B) Property-property plot of $\delta^{18}O$ and salinity, showing mixing lines between CDW and three different meteoric endmembers (left dotted, −20‰; middle solid, −25‰; and right dotted, −30‰). All depth-discrete $\delta^{18}O$ values are plotted, with light gray corresponding to surface values (0–20 m), dark gray, to values in the winter mixed layer (σ_θ < 27.5), and black, to values below the winter mixed layer. In $\delta^{18}O$-S space, melting (M) and freezing (F) of sea ice would move the data points almost horizontally, while mixing with CDW would move them diagonally upward to the right and mixing with pure meteoric water would move them diagonally downward to the left along the envelope prescribed by the mixing lines.

doi: 10.12952/journal.elementa.000065.f009

observed elsewhere (i.e., > 1.5%), with column inventories averaging around 8 m. In contrast, where upwelling or mixing of isotopically-heavier CDW into the WML occurred, as at the DIS outflow (Station 60; Figure 10A) and at the iceberg 'mixed' stations (Figures 10 E–G), meteoric fractions decreased and water column inventories of total meteoric water were slightly lower.

Consistent with the distribution of surface values in $\delta^{18}O$-S space discussed above (Figure 9B), a few locations exhibited positive sea ice melt fractions at the surface (Figure 10 J–K and O–P), indicating net sea ice melt. Otherwise throughout most of the ASP area, sea ice melt fractions were mostly negative throughout

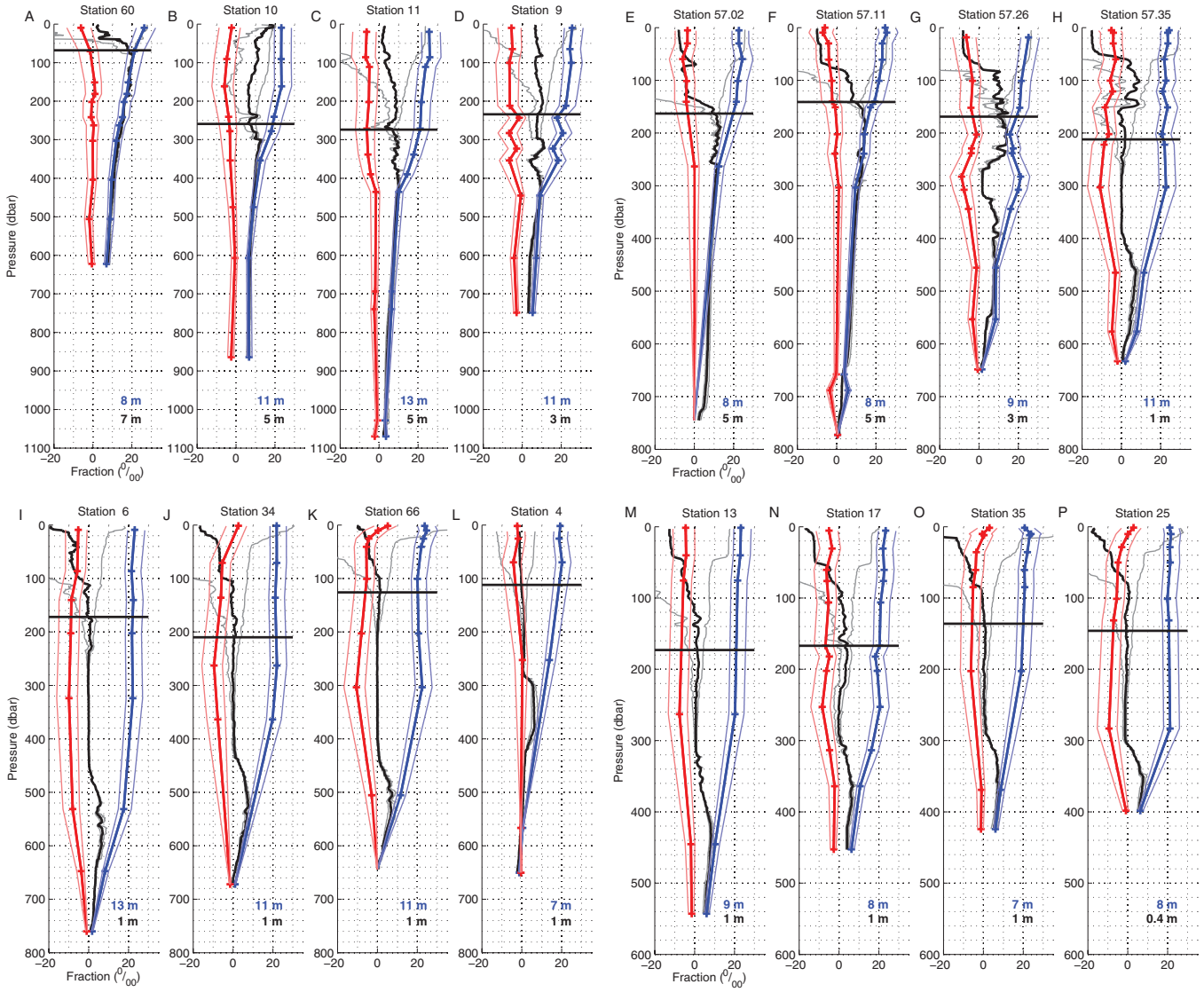

Figure 10

Vertical distributions of fractions of freshwater and of subsurface glacial meltwater by location.

Vertical profiles of freshwater fractions from meteoric (blue) and sea ice melt (red) sources derived from CTD discrete $\delta^{18}O$ data, together with vertical profiles of glacial meltwater fractions derived from CTD O_2-S (black), O_2-θ and θ-S (gray), for the following locations: (A–D) the DIS stations, located west/left (Station 60, outflow station) to east/right (Stations 10, 11 and 9); (E-H) locations in the vicinity of a drifting iceberg; waters not yet mixed by the drifting iceberg are captured by s57.35 (right), while waters mixed by the drifting iceberg are captured by the other s57 casts; (I–L) Stations 6, 34, 66 and 4, going from south mid-shelf to north at the shelf break; and (M-P) Stations 13, 17, 35 and 21, going from west to east onto the shallow bank north of Bear Peninsula. Bold blue/red profiles are based on a meteoric endmember of −25‰; light blue/red profiles (left/right of bold blue/red profiles) are based on −20‰ and −30‰, respectively. Negative fractions of sea ice melt indicate net sea ice production. The black horizontal line indicates the depth above which the glacial meltwater fractions were discounted and below which the subsurface column inventories are given. At the bottom of each subplot are listed the total column inventories of meteoric water (in blue; see also Figure 11A) and the subsurface column inventories of glacial meltwater (in black; see also Figure 12D). See Figure 11A & 12A for locations of station transects plotted in A–D, E–H, I–L, and M–P.

doi: 10.12952/journal.elementa.000065.f010

the water column, indicating net salinification due to net (annual) sea ice production. Geographic distributions of meteoric water column inventories (Figure 11A) showed that inventories were highest over the deep trough area, particularly in locations not experiencing upwelling or deep mixing. Inventories of sea ice melt were all negative and were highest in the mid-shelf trough area (Figure 11B).

Vertical profiles of the fractions of subsurface glacial meltwater (Figure 10, in black) also showed vertical and regional variability across the four representative areas. The effects of upwelling or mixing are clearly seen in the subsurface glacial meltwater profiles at all the DIS and iceberg-affected stations (Figure 10 A–G). In contrast, where there was little upwelling or mixing, a well-defined subsurface glacial meltwater maximum resided well below the surface layer along the 27.55–27.59 isopycnal (Figure 10 H, I–P; Figure 12B), which ranged in depth from ~ 600 m to 350 m (Figure 12C). The highest glacial meltwater maxima were at the

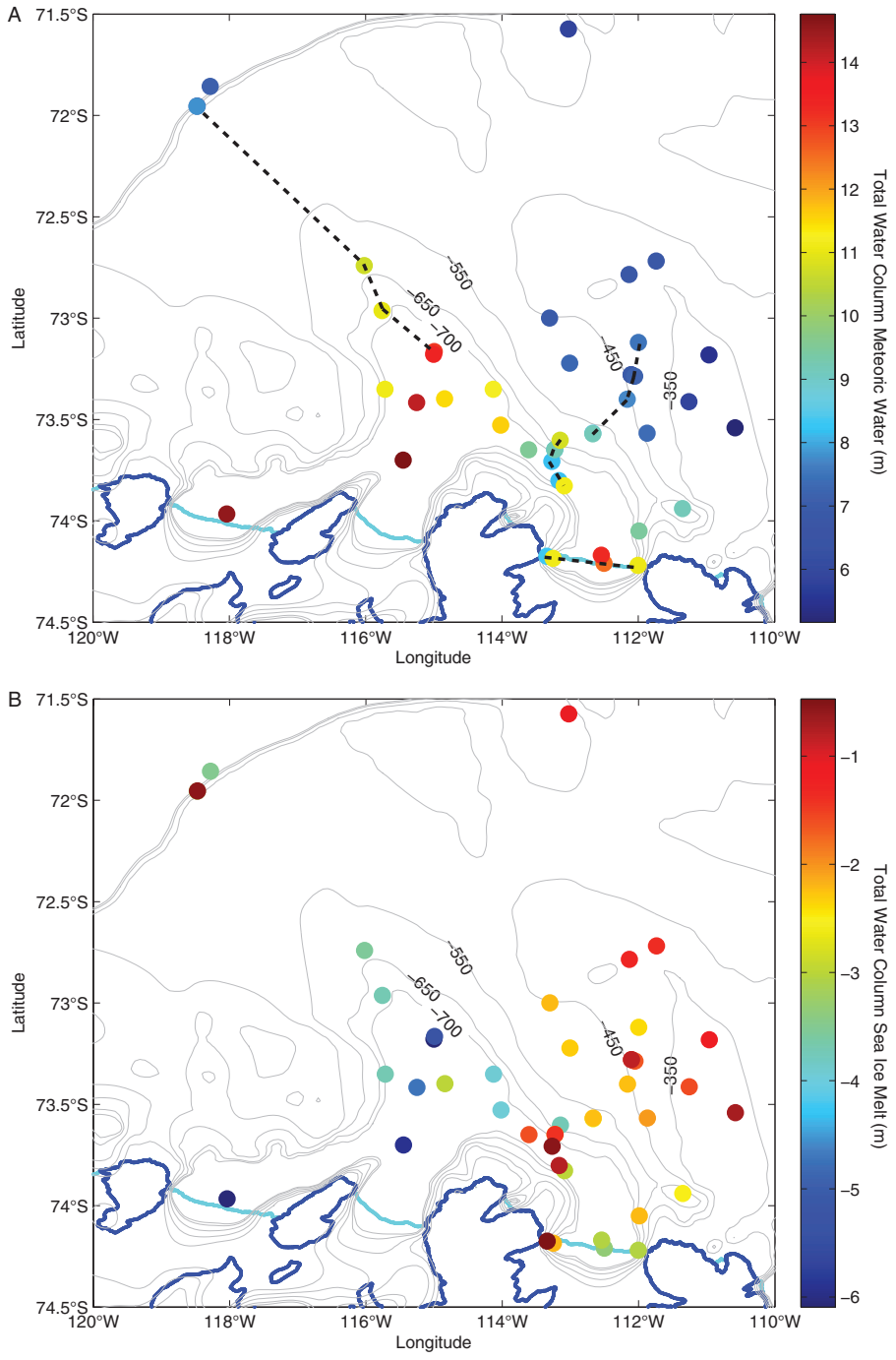

Figure 11

Regional distribution of $\delta^{18}O$-derived meteoric water and sea ice melt.

Column inventories (m) of (A) meteoric water, (B) sea ice melt, both derived from discrete $\delta^{18}O$ CTD data; negative values indicate net sea ice production. Bathymetry is from Nitsche et al. (2007); coastlines are from MOA2004 (Haran et al., 2013). The four dotted lines in (A) are the station transects plotted in Figure 10.

doi: 10.12952/journal.elementa.000065.f011

DIS outflow (2.1%; Figures 10A and 12A) and where there was upwelling or mixing (1.0–1.5%; Figures 10 B–D, E–H and 12A). Elsewhere, the glacial meltwater maxima were of moderate magnitudes (0.6–0.8%) (Figure 12A).

The column inventories of subsurface glacial meltwater (Figures 10 and 12D) were considerably higher where there was active upwelling, e.g., in front of the DIS and at the iceberg affected area (Figure 10 A–G). Nonetheless, the lower and deeper values are also important, as they indicate a distinct subsurface melt-laden layer throughout the ASP region that is available to deep mixing. However, and by default, the column inventories of subsurface glacial meltwater content were of lesser magnitude than the column inventories of total meteoric content (Figures 11A and 12 D) due to the fact that the subsurface column inventories were computed over a much smaller depth interval (i.e., from the subsurface black horizontal line in Figure 10 to the bottom of the cast).

We also note that the subsurface glacial meltwater estimates do not distinguish how much of the subsurface glacial meltwater originated from basal ice shelf melt or was generated locally by deep iceberg melt. Further, the portion of the subsurface glacial meltwater content originating in the DIS outflow that was detectable north of the DIS (by this method) was only that portion remaining below the mixed layer. Thus, we are unable to track upwelled glacial meltwater inputs (beyond the upwelled site) or the shallower inputs of glacial meltwater at the DIS outflow, except through their contributions to the total meteoric content. This issue is well illustrated by Figure 10, which shows the fractions of subsurface glacial meltwater in relation to the meteoric fractions (black and blue lines, respectively). Indeed, the portion of locally derived subsurface glacial

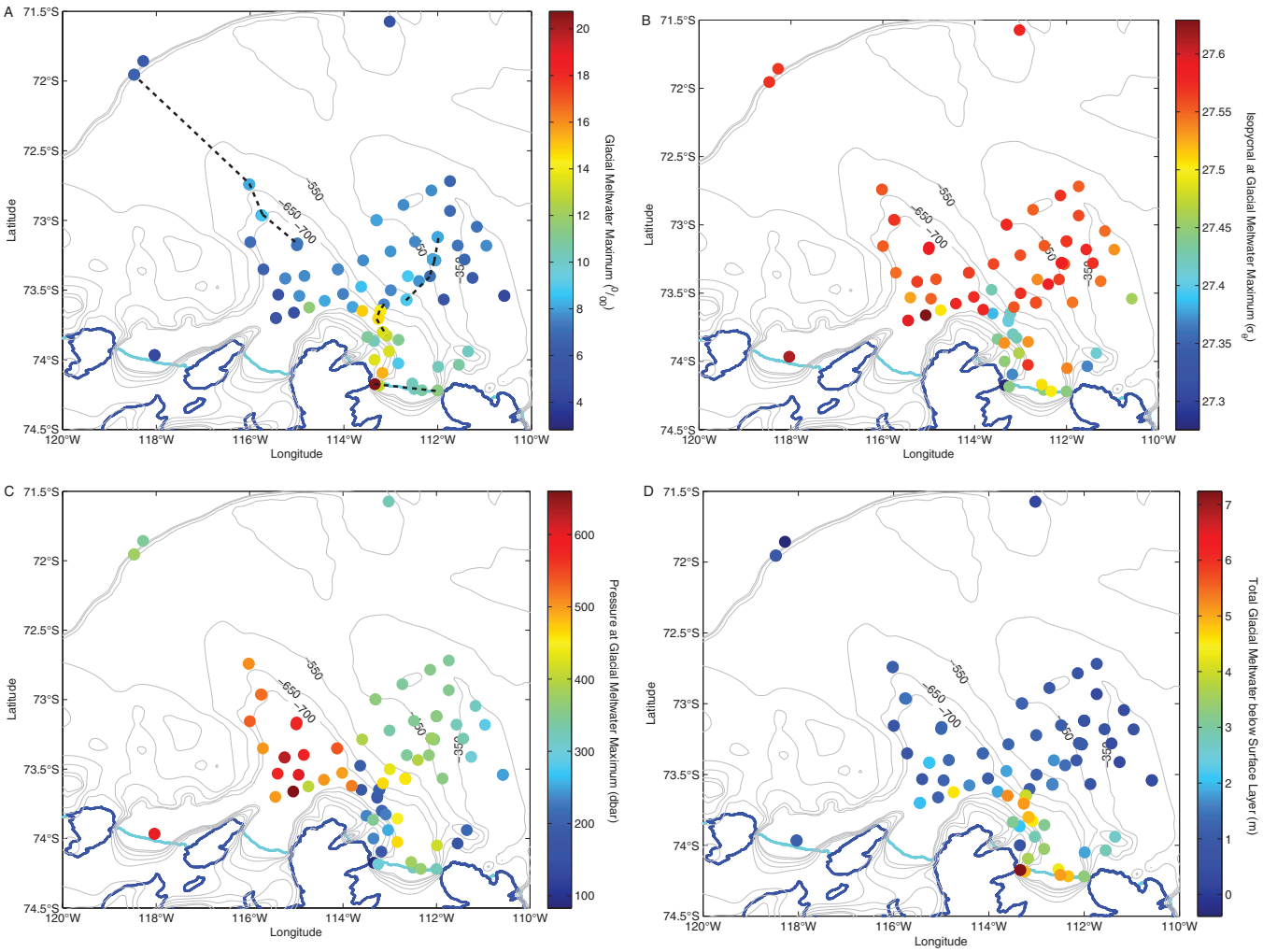

Figure 12

Regional and vertical distributions of subsurface glacial meltwater.

The subsurface glacial meltwater (A) maximum (‰), (B) σ_θ isopycnal at the maximum, (C) pressure (dbar) at the maximum, and (D) column inventories (m) of the total glacial meltwater below the surface layer. Bathymetry is from Nitsche et al. (2007); coastlines are from MOA2004 (Haran et al., 2013). The four dotted lines in (A) are the station transects plotted in Figure 10.

doi: 10.12952/journal.elementa.000065.f012

meltwater (e.g., from the DIS) that was mixed into the winter mixed layer is unknown by these approaches, but it is an inferred significant contributor to the relatively high meteoric content observed in the deep winter mixed layers. These interpretations, and the caveats of showing fractions of subsurface glacial meltwater along side meteoric fractions (Figure 10), are discussed in the next section.

Finally, we note that the fractions of meteoric, sea ice melt and subsurface glacial meltwater are relative to the endmembers used in our calculations. Specifically, these estimates are relative to CDW observed in the deep trough on the shelf and relative to the region-wide values used for sea ice melt and meteoric inputs. One effect of this relativity is that positive (non-zero) meteoric and glacial meltwater values were found at depth for the profiles located away from the deep trough area (e.g., Figure 10 A, B, D, M–P), where a more modified CDW is isotopically lighter relative to its less modified value deep in the trough. We also note that the accumulation of freshwater in the deep WMLs has likely occurred over time scales longer than a single season and that this freshwater originated from both local and non-local inputs.

Discussion

Assessing freshwater sources

We found that substantial meteoric water (7–13 m) accumulates in the deep WMLs of the ASP region. The largest amounts (11–13 m), found in front of the DIS and over the deep trough area, are approximately twice the amount reported for the rapidly-warming western Antarctic Peninsula region, where values of 4–6 m of meteoric water were found in the Marguerite Bay area (Meredith et al., 2010). The greater accumulation of meteoric water in the ASP region is made possible by WMLs being approximately twice as deep in the ASP area (as compared to Marguerite Bay) and by the large supply of meteoric water to this region.

The high accumulation of meteoric water in the deep WMLs is the net impact of both local and remote freshwater sources. Key to interpreting our results is the acknowledgement that the estimated freshwater content reflects contributions made over large spatial and temporal scales. That the sea ice meltwater fractions are largely negative, for example, indicates that this region is a net sea ice producer, even if some local sea ice melt had occurred during the few weeks prior to our sampling. Further, some of the accumulated meteoric water comes not only from basal ice shelf melt upwelled in front of the DIS, but also from basal ice shelf melt upwelled in front of ice shelves upstream (east) of the DIS (e.g., Crosson, Thwaites, Pine Island) (e.g., Jacobs et al., 2011; Mankoff et al., 2012), or from icebergs within the TFIT and elsewhere upstream. The glacial meltwater inputs upstream of the DIS are carried westward into the ASP region by the surface circulation (Assmann et al., 2005). Additional glacier meltwater comes from numerous icebergs drifting through the ASP, as well as from seasonal glacier melt at the air-ice-ocean boundary by open waters warmed by solar insolation. Added to these sources is the accumulation of precipitation inputs to the WML, both locally and remotely, the latter carried into the ASP by the surface circulation. In the overall freshwater budget for the ASP region, these local and non-local inputs are then partially compensated by the salinification due to net sea ice production, such as typifies this polynya area.

The subsurface glacial meltwater estimates as quantified in Figures 10 and 12 are those contributions from deep melting and upwelling to the total meteoric estimates as quantified in Figures 10 and 11. However, the glacial meltwater estimates from basal melt of ice shelves and icebergs can only be detected subsurface (with the approach used here). Thus, how much of the upwelled basal ice shelf and iceberg meltwater contributed to the total meteoric content is unknown; we infer that the contribution is significant based on the following.

The highest maximum meteoric concentrations, reaching 2.6%, were observed near the surface in front of the DIS outflow (Station 60) and at DIS Station 11 (mid-ice-shelf) (Figure 10 A, C). Because these observations were coincident with supersaturated pCO_2 and low dissolved oxygen at the sea surface (Mu et al., 2014), they likely represent upwelled deep waters made buoyant by glacial meltwater. The highest subsurface glacier meltwater concentration was 2.1% and was observed at the DIS outflow (Station 60) at a depth of 82 m, i.e., just before the signal was lost to surface contamination. Although we cannot explicitly determine how much of the higher meteoric content at the surface was derived from upwelled basal ice shelf melt versus surface meltwater inputs, the dissolved gases corroborate that the major contributor is basal ice shelf melt.

Rignot et al. (2013) estimated that the DIS discharges approximately 45.2 Gt of basal meltwater per year (as observed over 2003 to 2008). We estimated the western DIS outflow in December 2010 to be approximately 0.17 Sv (or 5.4×10^{12} m^3 yr^{-1}). Over the depth interval of this outflow (~ 100–400 m), the average glacial meltwater fraction is approximately 1.5%. This fraction equates to 8.1×10^{10} m^3 yr^{-1} of pure meltwater in the DIS outflow, or 81 Gt yr^{-1}. This instantaneous estimate is nearly twice as high as the 5-year average from Rignot et al. (2013) and likely reflects seasonal and yearly variability inferred from CDW temperature observations (Figure 2). However, the CDW temperature in December 2010 was near average for the year of deployment; thus, this higher estimate could also reflect an overall increase in discharge. Volume losses from Antarctic ice shelves appear to be accelerating (Paolo et al., 2015), with losses from West Antarctic ice shelves increasing by 70% in just the last decade. Thus, the DIS may be contributing upwards of 81 Gt yr^{-1} of basal meltwater to the ASP region since ~ 2010.

Variability in freshwater inputs to the ASP and biological productivity

A key question is whether spatial or temporal variability in the supply of the glacial meltwater impacts biological productivity. The ASP is not only the most productive polynya (per square meter), but its productivity is also the most variable (Arrigo and van Dijken, 2003), raising the issue of whether this biological variability could be linked to variable meltwater inputs. Previous studies have shown considerable temporal variability in basal ice shelf melt in the Amundsen Sea embayment region linked to variability in CDW properties accessing the ice shelf cavities (Jacobs et al., 2011, 2013; Dutrieux et al., 2014). In turn, temporal variability in CDW properties on the continental shelf has been linked to variability in atmospheric forcing.

Atmospheric forcing in this region is largely driven by the Amundsen Sea Low (ASL), which migrates seasonally. In summer, with the ASL north of the continental shelf, the dominant winds at the shelf break are southeasterly winds. In late winter to early spring, the ASL shifts to the southwest, causing the dominant winds near the shelf break to become northwesterly (Steig et al., 2012; Turner et al., 2013). Thus, winter–spring conditions tend to enhance CDW inflow onto the continental shelf (Thoma et al., 2008), through the strengthening of an undercurrent associated with the Antarctic Slope Front that transports CDW into the trough areas at the shelf break (Walker et al., 2013). The annual migration of the ASL, however, is highly variable and sensitive to atmospheric perturbations caused by the Southern Annular Mode (SAM) (e.g., Turner et al., 2013) and by tropical teleconnections such as the El Niño Southern Oscillation (ENSO) (e.g., Steig et al., 2012; Turner et al., 2013) and the Atlantic Multidecadal Oscillation (Li et al., 2014). These various factors contribute to the high seasonal and interannual variability of CDW moving onto the continental shelf (Jacobs et al., 2012; Dutrieux et al., 2014). Time series of near-bottom temperatures from moorings in front of the DIS (Jacobs et al., 2012) (Figure 2) are also consistent with these observations.

Seasonal variability also occurs in other mechanisms that contribute freshwater to the deep WMLs of the ASP region. In fall–winter in the central ASP (i.e., distant from the variable but near continuous upwelling occurring at the DIS), inputs of subsurface glacial meltwater occur through entrainment from brine-induced mixing during sea ice production, whereas in spring–summer, they occur through solar surface warming. However, strong wind events during the spring–summer opening of the ASP could also potentially mix melt-laden CDW vertically, particularly where the subsurface glacial meltwater maximum shoals in the shallower areas, e.g., north of the DIS outflow and east over the shallow bank area (Figure 12C). Coastal-derived meltwater may also be continually mixed by tides (Robertson, 2013), as well as advected into the ASP by eddies generated in the coastal current, that in turn transport and diffuse the glacial meltwater offshore (Spall et al., 2008; St-Laurent et al., 2014).

The DIS outflow was enriched in dissolved iron (dFe) compared to the central polynya (Sherrell et al., 2015). The dFe enrichment is hypothesized to be derived from continental material released during basal ice shelf melt, but may also have been derived from sediments near the grounding line or where the outflow interacts with sediments along the western margin of the ice cavity (Sherrell et al., 2015). Elevated dFe at the DIS outflow and at specific depths in the WML throughout the ASP is consistent with the idea that the DIS outflow is a major contributor of Fe-enriched meltwater. A key question related to potential biological impacts is how much of the Fe-enriched meltwater exiting the DIS is delivered to the euphotic zone of the ASP, particularly to the shallow bank area, and by what mechanism.

The eastern bank area, comprising the central ASP, was characterized by high biological activity, with observed chlorophyll *a* values > 15 mg m^{-3} (versus < 15 mg m^{-3} over the deep trough areas) (Alderkamp et al., 2015). The areas with the highest primary productivity were accompanied by low surface CO_2 concentrations (< 170 ppm) and high surface oxygen (10.8 mL L^{-1}), indicative of enhanced biological drawdown and production (Mu et al., 2015). To support such high productivity, the ASP must be fueled by a quasi-continuous supply of bioavailable Fe. As described above, this supply is likely accomplished by winter entrainment of subsurface Fe-enriched glacial meltwater, and more continuously by deep wind mixing and iceberg stirring, bringing subsurface meltwater to the euphotic zone over the course of the bloom period. Finally, eddy activity may transport additional Fe-enriched melt-laden waters from the coastal current northward into the central ASP. All of these delivery mechanisms are sensitive to climate change (as discussed next), with potentially contrasting influences on Fe availability and thus biological productivity.

A rapidly changing environment

The Amundsen Sea is changing rapidly in terms of losses of glacial ice mass along its coast (Pritchard et al., 2012) and of sea ice north of its coast (Jacobs and Comiso, 1997; Stammerjohn et al., 2012, 2015). Sea ice changes over the period of 1979–2013 have resulted in a lengthening of the open water season by ~ 2.6 months in the ASP area, due primarily to an earlier spring opening by ~ 2.2 months (Stammerjohn et al., 2015). These changes allow more solar radiation and potentially more surface melt to enter the ASP, but also more wind mixing as well; these are competing factors that alter water column stratification and the delivery of Fe-enriched meltwaters to the euphotic zone, with consequent impacts on primary production.

In the Amundsen Sea, ice shelf thinning and grounding line retreat have been linked to an increasing presence of warmer CDW on the continental shelf, driving a more intensified circulation under the ice

shelves (Jenkins et al., 2010; Jacobs et al., 2011; Dutrieux et al., 2014). Currently, estimates of basal ice shelf melt and calving fluxes in the Amundsen Sea embayment are some of the highest observed anywhere in coastal Antarctica (Rignot et al., 2013; Paolo et al., 2015). If the strengthened westerly winds (Bracegirdle, 2013) persist, as well as the increases in deep ocean heat content on the continental shelf (Martinson et al., 2008; Jacobs et al., 2011; Martinson, 2012), then there will likely be sufficient ocean heat delivered to the ice shelf cavities in the Amundsen Sea embayment to drive continued or even increased basal ice shelf melt and grounding line retreat. The Thwaites Glacier in particular is experiencing a rapid grounding line retreat (Mouginot et al., 2014), along with rapid changes to its glacier tongue (MacGregor et al., 2012). Given these changes, icebergs may become a more significant factor in distributing glacial meltwaters in the ASP.

These climate-sensitive meltwater changes in the ASP will continue to have a strong influence on the biogeochemistry and biology of the ASP, yet there are many unanswered questions. For example, how will the vertical distribution of freshwater change in the future, with increased meltwater inputs, both at depth and at the surface? What will be the response to increased winds versus increased surface freshwater inputs in regard to stratification and the availability of Fe? How will Fe-enriched meltwater sources and the delivery of Fe to the euphotic zone change? Progress in answering these questions is underway with ongoing studies focused on ocean-ice shelf interactions.

Summary

Here we present results from a densely-sampled hydrographic survey of the Amundsen Sea Polynya (ASP) region, including a detailed characterization of its freshwater distribution. Our survey extended from the Dotson Ice Shelf (DIS) north to the continental shelf break and included both the deep Dotson trough (~ 600–1200 m) that bisects the continental shelf and the shallow bank (150–300 m) east of the trough that lies adjacent to, and west of, the Thwaites Fast ice and Iceberg Tongue (TFIT). To spatially and vertically resolve different contributions to the freshwater budget, we first quantified inputs from sea ice melt and from meteoric-derived sources using stable oxygen isotope ratios in seawater ($\delta^{18}O$). Meteoric sources include direct precipitation and glacial melt from both local and non-local sources. We then separately quantified glacial meltwater inputs entrained into Circumpolar Deep Water (CDW) at depth either from basal ice shelf melt or from iceberg melt. We summarize the results as follows.

- A hydrographic survey along the length of the DIS front showed a melt-laden outflow of CDW emanating from under the DIS, with strongest flows concentrated at its western end.
- Observed ocean currents showed northward flow of the melt-laden CDW along the deep trough region, as well as into the shallow ASP area (the former is consistent with previous observations of topographically steered meltwater outflow along troughs) (St-Laurent et al., 2013; Wåhlin et al., 2013).
- Vertical distributions of meteoric fractions (following Meredith et al., 2013) showed maximum values ranging from 2 to 3% in the deep (300–400 m) winter mixed layers (WMLs), with highest fractions in the top 100–200 m.
- Given the deep WMLs, column inventories of meteoric water were high, ranging from 10–13 m adjacent to the DIS and in the deep trough, and from 7–9 m in shallower areas; the former were twice those reported for continental shelf waters near the western Antarctic Peninsula.
- Sea ice melt fractions were mostly negative, indicating net freshwater extraction (i.e., salinification) due to net (annual) sea ice production, consistent with this area being an active polynya.
- The separately determined fractions of subsurface glacial meltwater (following Jenkins, 1999) showed maximum values ranging from 1 to 2%; fractions were highest (2.1%) and shallowest (80–90 m) at the DIS outflow and in waters perturbed by a drifting iceberg (1.5% and 150–200 m, respectively).
- Observations near a drifting iceberg showed vertical mixing of CDW, laden with meltwater, thus indicating that drifting icebergs, which frequent the ASP region (typically breaking free of the TFIT and then drifting westward across the ASP), are important mechanisms for vertically mixing melt-laden waters.
- Away from the DIS and drifting iceberg, the fractions of subsurface glacial meltwater indicated a melt-laden layer along the ~ 27.6 isopycnal; from this depth subsurface glacial meltwater can be entrained into the mixed layer each winter from brine-induced mixing during sea ice production, and each spring–summer through wind mixing, tidal mixing, iceberg stirring and eddies, the latter 'diffusing' the freshwater offshore (Spall et al., 2008; St-Laurent et al., 2014).
- Although we cannot determine explicitly how much of the relatively high meteoric content in the ASP region was derived from DIS basal ice shelf melt, given the strong melt-laden outflow at the western end of the DIS (estimated to be 0.17 Sv discharging 81 Gt yr^{-1} of pure meltwater), we infer that DIS basal meltwater is a major contributor to the freshwater budget in the ASP region.
- Our results suggest a quasi-continuous supply of melt-laden iron-enriched seawater to the euphotic zone of the ASP, which helps to explain why the ASP is Antarctica's most productive polynya per unit area.

References

Alderkamp A-C, Dijken GL, Lowry KE, Connelly TL, Lagerstrom M, et al. 2015. Fe availability drives phytoplankton photosynthesis rates in the Amundsen Sea Polynya, Antarctica. *Elem Sci Anth* **3**: 000043. doi:10.12952/journal.elementa.000043.

Arneborg L, Wåhlin AK, Björk G, Liljebladh B, Orsi AH. 2012. Persistent inflow of warm water onto the central Amundsen shelf. *Nat Geosci* **5**: 876–880. doi:10.1038/ngeo1644.

Arrigo KR, Lowry KE, van Dijken GL. 2012. Annual changes in sea ice and phytoplankton in polynyas of the Amundsen Sea, Antarctica. *Deep-Sea Res Pt II* **71–76**: 5–15. doi:10.1016/j.dsr2.2012.03.006.

Arrigo KR,van Dijken GL. 2003. Phytoplankton dynamics within 37 Antarctic coastal polynya systems. *J Geophys Res* **108**: doi:10.1029/2002jc001739.

Assmann KM, Hellmer HH, Jacobs SS. 2005. Amundsen Sea ice production and transport. *J Geophys Res* **110**: doi:10.1029/2004jc002797.

Bracegirdle TJ. 2013. Climatology and recent increase of westerly winds over the Amundsen Sea derived from six reanalyses. *Int J Climatol* **33**: 843–851. doi:10.1002/joc.3473.

Bromwich DH, Nicolas JP, Monaghan AJ, Lazzara MA, Keller LM, et al. 2012. Central West Antarctica among the most rapidly warming regions on Earth. *Nat Geosci* **6**: 139–145. doi:10.1038/ngeo1671.

Coplen TB. 1994. Reporting of stable hydrogen, carbon, and oxygen isotopic abundances. *Pure Appl Chem* **66**: 273–276.

Ducklow HW, Wilson SE, Post AF, Stammerjohn SE, Erickson M, et al. 2015. Particle flux on the continental shelf in the Amundsen Sea Polynya and western Antarctic Peninsula. *Elem Sci Anth* **3**: 000046. doi:10.12952/journal.elementa.000046.

Dutrieux P, De Rydt J, Jenkins A, Holland PR, Ha HK, et al. 2014. Strong sensitivity of Pine Island ice-shelf melting to climatic variability. *Science* **343**: 174–178. doi:10.1126/science.1244341.

Epstein S, Mayeda T. 1953. Variation of oxygen-18 content of waters from natural sources. *Geochim Cosmochim Acta* **4**: 213–224.

Fairbanks RG. 1982. The origin of continental shelf and slope water in the New York Blight and Gulf of Maine: evidence from $H_2{}^{18}O/H_2{}^{16}O$ ratio measurements. *J Geophys Res* **87**: 5796–5808.

Fransson A, Chierici M, Yager PL, Smith WO. 2011. Antarctic sea ice carbon dioxide system and controls. *J Geophys Res* **116**: doi:10.1029/2010jc006844.

Fraser AD, Massom RA, Michael KJ, Galton-Fenzi BK, Lieser JL. 2012. East Antarctic landfast sea ice distribution and variability, 2000–08. *J Clim* **25**: 1137–1156. doi: 10.1175/JCLI-D-10-05032.1.

Haran T, Bohlander J, Scambos T, Painter T, Fahnestock M. 2013. MODIS Mosaic of Antarctica 2003–2004 (MOA2004) Image Map [Coastlines, Grounding Lines, and Islands]. doi: 10.7265/N5ZK5DM5.

Haran T, Bohlander J, Scambos T, Painter T, Fahnestock M. 2014. MODIS Mosaic of Antarctica 2008–2009 (MOA2009) Image Map [Coastlines, Grounding Lines, and Islands]. doi: 10.7265/N5KP8037.

Hellmer HH, Jacobs SS, Jenkins A. 1998. Oceanic erosion of a floating Antarctic glacier in the Amundsen Sea, in Jacobs SS, Weiss RF, eds., *Ocean, Ice, and Atmosphere: Interactions at the Antarctic Continental Margin*, vol. 75. Washington DC: American Geophysical Union: pp. 83–99.

Jacobs S, Giulivi C, Dutrieux P, Rignot E, Nitsche F, et al. 2013. Getz Ice Shelf melting response to changes in ocean forcing. *J Geophys Res-Oceans* **118**: 4152–4168. doi:10.1002/jgrc.20298.

Jacobs SS, Comiso JC. 1997. Climate variability in the Amundsen and Bellingshausen Seas. *J Clim* **10**: 697–709.

Jacobs SS, Jenkins A, Giulivi CF, Dutrieux P. 2011. Stronger ocean circulation and increased melting under Pine Island Glacier ice shelf. *Nat Geosci* **4**: 519–523. doi:10.1038/ngeo1188.

Jacobs SS, Jenkins A, Hellmer H, Giulivi C, Nitsche F, et al. 2012. The Amundsen Sea and the Antarctic Ice Sheet. *Oceanography* **25**: 154–163. doi:10.5670/oceanog.2012.90.

Jenkins A. 1999. The Impact of Melting Ice on Ocean Waters. *J Phys Oceanogr* **29**: 2370–2381.

Jenkins A, Dutrieux P, Jacobs SS, McPhail SD, Perrett JR, et al. 2010. Observations beneath Pine Island Glacier in West Antarctica and implications for its retreat. *Nat Geosci* **3**: 468–472. doi: 10.1038/ngeo890.

Jenkins A, Jacobs S. 2008. Circulation and Melting Beneath George VI Ice Shelf, Antarctica. *J Geophys Res* **113**. doi:10.1029/2007jc004449.

Joughin I, Alley RB. 2011. Stability of the West Antarctic ice sheet in a warming world. *Nat Geosci* **4**: 506–513.

Knap A, Michaels A, Close A, Ducklow HW, Dickson A. 1996. Protocols for the Joint Global Ocean Flux Study (JGOFS) Core Measurements. JGOFS, Reprint of the IOC Manuals and Guides No. 29, UNESCO 1994, Report No. 19.

Li X, Holland DM, Gerber EP, Yoo C. 2014. Impacts of the north and tropical Atlantic Ocean on the Antarctic Peninsula and sea ice. *Nature* **505**: 538–542. doi:10.1038/nature12945.

MacGregor JA, Catania GA, Markowski MS, Andrews AG. 2012. Widespread rifting and retreat of ice-shelf margins in the eastern Amundsen Sea Embayment between 1972 and 2011. *J Glaciol* **58**: 458–466. doi:10.3189/2012JoG11J262.

Mankoff KD, Jacobs SS, Tulaczyk SM, Stammerjohn SE. 2012. The role of Pine Island Glacier ice shelf basal channels in deep-water upwelling, polynyas and ocean circulation in Pine Island Bay, Antarctica. *Ann Glaciol* **53**: 123–128. doi:10.3189/2012AoG60A062.

Martinson DG. 2012. Antarctic circumpolar current's role in the Antarctic ice system: An overview. *Paleogeog Paleoclim Paleoecol*. doi:10.1016/j.palaeo.2011.04.007.

Martinson DG, Stammerjohn SE, Iannuzzi RA, Smith RC, Vernet M. 2008. Palmer, Antarctica, Long-Term Ecological Research program first twelve years: Physical oceanography, spatio-temporal variability. *Deep-Sea Res Pt II* **55**: 1964–1987. doi:10.1016/j.dsr2.2008.04.038.

Massom RA, Hill KL, Lytle VI, Worby AP, Paget MJ, et al. 2001. Effects of regional fast-ice and iceberg distributions on the behavior of the Mertz Glacier polynya, East Antarctica. *Ann Glaciol* **33**: 391–398.

Meredith MP, Brandon MA, Wallace MI, Clarke A, Leng MJ, et al. 2008. Variability in the freshwater balance of northern Marguerite Bay, Antarctic Peninsula: Results from $\delta^{18}O$. *Deep-Sea Res Pt II* **55**: 309–322. doi:10.1016/j.dsr2.2007.11.005.

Meredith MP, Venables HJ, Clarke A, Ducklow HW, Erickson M, et al. 2013. The freshwater system west of the Antarctic Peninsula: Spatial and temporal changes. *J Clim* **26**: 1669–1684. doi:10.1175/jcli-d-12-00246.1.

Meredith MP, Wallace MI, Stammerjohn SE, Renfrew IA, Clarke A, et al. 2010. Changes in the freshwater composition of the upper ocean west of the Antarctic Peninsula during the first decade of the 21st century. *Progr Oceanogr* **87**: 127–143. doi:10.1016/j.pocean.2010.09.019.

Mouginot J, Rignot E, Scheuchl B. 2014. Sustained increase in ice discharge from the Amundsen Sea Embayment, West Antarctica, from 1973 to 2013. *Geophys Res Lett* **41**: 1576–1584. doi:10.1002/2013gl059069.

Mu L, Stammerjohn SE, Lowry KE, Yager PL. 2014. Spatial variability of surface pCO_2 and air-sea CO_2 flux in the Amundsen Sea Polynya, Antarctica. *Elem Sci Anth* **2**: 000036. doi:10.12952/journal.elementa.000036.

Nihashi S, Ohshima KI. 2015. Circumpolar mapping of Antarctic coastal polynyas and landfast sea ice: Relationship and variability. *J Clim* **28**: **3650**–3670. doi:10.1175/JCLI-D-14-00369.1.

Nitsche FO, Jacobs SS, Larter RD, Gohl K. 2007. Bathymetry of the Amundsen Sea continental shelf: Implications for geology, oceanography, and glaciology. *Geochem Geophys Geosyst* **8**: 1–10. doi:10.1029/2007gc001694.

Östlund HG, Hut G. 1984. Arctic Ocean water mass balance from isotope data. *J Geophys Res* **89**: 6373–6381.

Paolo FS, Fricker HA, Padman L. 2015. Volume loss from Antarctic ice shelves is accelerating. *Science*. doi:10.1126/science.aaa0940.

Potter JR, Talbot MH, Paren JG. 1988. Oceanic regimes at the ice fronts of George VI Sound, Antarctic Peninsula. *Cont Shelf Res* **8**: 347–362.

Pritchard HD, Arthern RJ, Vaughan DG, Edwards LA. 2009. Extensive dynamic thinning on the margins of the Greenland and Antarctic ice sheets. *Nature* **461**: 971–975. doi:10.1038/nature08471.

Pritchard HD, Ligtenberg SR, Fricker HA, Vaughan DG, van den Broeke MR, et al. 2012. Antarctic ice-sheet loss driven by basal melting of ice shelves. *Nature* **484**: 502–505. doi:10.1038/nature10968.

Randall-Goodwin E. 2012. Detecting Meltwater in the Amundsen Sea Polynya Region, West Antarctica. *Master's Thesis*, University of California Santa Cruz.

Rignot E, Jacobs S, Mouginot J, Scheuchl B. 2013. Ice-shelf melting around Antarctica. *Science* **341**: 266–270. doi:10.1126/science.1235798.

Rignot E, Mouginot J, Morlighem M, Seroussi H, Scheuchl B. 2014. Widespread, rapid grounding line retreat of Pine Island, Thwaites, Smith, and Kohler glaciers, West Antarctica, from 1992 to 2011. *Geophys Res Lett* **41**: 3502–3509. doi:10.1002/2014gl060140.

Robertson R. 2013. Tidally induced increases in melting of Amundsen Sea ice shelves. *J Geophys Res: Oceans* **118**: 3138–3145. doi:10.1002/jgrc.20236.

Sherrell RM, Lagerstrom M, Forsch KO, Stammerjohn SE, Yager PL. 2015. Dynamics of dissolved iron and other bioactive trace metals (Mn, Ni, Cu, Zn) in the Amundsen Sea Polynya, Antarctica. *Elem Sci Anth*: Under review for this Special Feature.

Spall MA, Pickart RS, Fratantoni PS, Plueddemann AJ. 2008. Western Arctic shelfbreak eddies: Formation and transport. *J Phys Oceanogr* **38**: 1644–1668.

St-Laurent P, Klinck JM, Dinniman MS. 2013. On the role of coastal troughs in the circulation of warm Circumpolar Deep Water on Antarctic shelves. *J Phys Oceanogr* **43**: 51–64. doi:10.1175/jpo-d-11-0237.1.

St-Laurent P, Klinck JM, Dinniman MS. 2014. Vertical and horizontal transport by mesoscale eddies in the Amundsen Sea: Where, when, and how much. Ocean Sciences. Honolulu, HI. February 23–28.

Stammerjohn S, Massom R, Rind D, Martinson D. 2012. Regions of rapid sea ice change: An inter-hemispheric seasonal comparison. *Geophys Res Lett* **39**: L06501. doi:10.1029/2012gl050874.

Stammerjohn SE, Maksym T, Massom RA, Lowry KE, Arrigo KR, et al. 2015. Seasonal sea ice changes in the Amundsen Sea, Antarctica. *Elem Sci Anth*: **3**: 000055. doi: 10.12952/journal.elementa.000055.

Steig EJ, Ding Q, Battisti DS, Jenkins A. 2012. Tropical forcing of Circumpolar Deep Water inflow and outlet glacier thinning in the Amundsen Sea Embayment, West Antarctica. *Ann Glaciol* **53**: 19–28. doi:10.3189/2012AoG60A110.

Steig EJ, Schneider DP, Rutherford SD, Mann ME, Comiso JC, et al. 2009. Warming of the Antarctic ice-sheet surface since the 1957 International Geophysical Year. *Nature* **457**: doi:10.1038/nature07669.

Thoma M, Jenkins A, Holland D, Jacobs S. 2008. Modelling Circumpolar Deep Water intrusions on the Amundsen Sea continental shelf, Antarctica. *Geophys Res Lett* **35**: doi:10.1029/2008gl034939.

Turner J, Phillips T, Hosking JS, Marshall GJ, Orr A. 2013. The Amundsen Sea low. *Int J Climatol* **33**: 1818–1829. doi:10.1002/joc.3558.

Wåhlin AK, Kalén O, Arneborg L, Björk G, Carvajal GK, et al. 2013. Variability of warm deep water inflow in a submarine trough on the Amundsen Sea shelf. *J Phys Oceanogr* **43**: 2054–2070. doi:10.1175/jpo-d-12-0157.1.

Wåhlin AK, Muench RD, Arneborg L, Björk G, Ha HK, et al. 2012. Some implications of Ekman layer dynamics for cross-shelf exchange in the Amundsen Sea. *J Phys Oceanogr* **42**: 1461–1474. doi:10.1175/jpo-d-11-041.1.

Wåhlin AK, Yuan X, Björk G, Nohr C. 2010. Inflow of warm Circumpolar Deep Water in the Central Amundsen Shelf. *J Phys Oceanogr* **40**: 1427–1434. doi:10.1175/2010jpo4431.1.

Walker DP, Jenkins A, Assmann KM, Shoosmith DR, Brandon MA. 2013. Oceanographic observations at the shelf break of the Amundsen Sea, Antarctica. *J Geophys Res: Oceans* **118**: 2906–2918. doi:10.1002/jgrc.20212.

Yager P, Sherrell R, Stammerjohn S, Alderkamp A-C, Schofield O, et al. 2012. ASPIRE: The Amundsen Sea Polynya International Research Expedition. *Oceanography* **25**: 40–53. doi:10.5670/oceanog.2012.73.

Contributions

- Contributed to conception and design: ERG, SS, RS, PY, ACA, PA, RG, KG
- Contributed to acquisition of data: ERG, SS, RG, PA, RS, PY, ACA, KG, RM
- Contributed to analysis and interpretation of data: (all)
- Drafted and/or revised the article: (all)
- Approved the submitted version for publication: (all)

Acknowledgments

We thank the captain and crew of the NBP and the U.S. Antarctic Program contractors for their invaluable assistance throughout the research cruise. We also thank "Oden Southern Ocean", SWEDARP 2010/11, organized by the Swedish Polar Research Secretariat and National Science Foundation Office of Polar Programs. Special thanks go to Jules Hummon and Eric Firing (University of Hawaii) for providing, calibrating and post-correcting the SADCP data. We also thank the National Snow and Ice Data Center (http://nsidc.org) and the Polar Geospatial Center (http://www.pgc.umn.edu/) for providing near-real time high-resolution satellite images during the field campaign critical for deciding sampling logistics. Finally, we thank NASA for providing the Rapid Response MODIS images through EOSDIS (Earth Observing System Data and Information System; http://lance-modis.eosdis.nasa.gov/) critical for determining the drifting iceberg locations. We also wish to thank the Editors and 3 anonymous reviewers for their helpful and constructive comments on earlier drafts.

Funding information

This project was funded by the National Science Foundation Office of Polar Programs within the division of Antarctic Organisms and Ecosystems (ANT-0838975 to SS/ERG, ANT- 0944727 to ACA, ANT-0838995 to RS, ANT-0839069 to PY, ANT-0839012 to HWD), with additional support from ANT-1440435 to HWD, SS, EG.

Competing interests

The authors have declared that no competing interests exist.

Data accessibility statement

All hydrographic data will be posted to NODC.